The Structure of the Free Neutron at Large x-Bjorken

A 12 GeV Research Proposal to Jefferson Lab (PAC 30)

M. Amarian, S. Bültmann (co-spokesperson)*, G. E. Dodge, C. E. Hyde-Wright, H. Juengst, S. E. Kuhn (co-spokesperson), S. Tkachenko, L. B. Weinstein, J. Zhang

Old Dominion University, Norfolk, Virginia, USA

V. Burkert, A. Deur, R. Ent, H. Fenker (co-spokesperson), W. Melnitchouk (co-spokesperson), S. Stepanyan

Jefferson Lab, Newport News, Virginia, USA

M. E. Christy (co-spokesperson), C. E. Keppel (co-spokesperson), V. Tvaskis (co-spokesperson)

Hampton University, Hampton, Virginia, USA

N. Kalantarians

University of Houston, Houston, Texas, USA

P.M. King, J.C. Peng

University of Illinois at Urbana-Champaign, Urbana-Champaign, Illinois, USA

K. L. Giovanetti, G. Niculescu, I. Niculescu

James Madison University, Harrisonburg, Virginia, USA

D. Dutta

Mississippi State University, Mississippi State, Mississippi, USA

N. Baillie, K. A. Griffioen (co-spokesperson)

The College of William and Mary, Williamsburg, Virginia, USA

and The CLAS Collaboration

* Contact: Stephen Bueltmann, Department of Physics, Old Dominion University, Norfolk, VA 23529. Email: stephenb@physics.odu.edu

Abstract

Understanding the structure of the nucleon is one of the fundamental goals of nuclear and high-energy physics. Deep-inelastic lepton scattering off proton and nuclear targets has produced a large amount of accurate data on the proton structure function, but not to the same extent on that of the neutron. Because of the instability of the free neutron, its structure is inferred from comparative measurements between nuclear targets, like deuterium, and proton targets. The precision of these measurements is limited because of the theoretical uncertainties introduced by nuclear models needed to extract information from the bound nucleons in the nuclei.

The BONUS collaboration (experiment E03-012) measured the neutron structure in the Fall of 2005 by scattering electrons of up to 5.3 GeV energy on a thin deuterium gas target and detecting the low-momentum recoiling spectator protons in the vicinity of that target. By constraining the spectator proton to very low momenta and very backward scattering angles, electron scattering events on almost free neutrons could be selected.

We propose an extension of this measurement of the inclusive electron scattering cross section on an almost free neutron using the upgraded CEBAF Large Acceptance Spectrometer (CLAS12) and the exisiting recoil detector instead of the central silicon vertex detector. The recoil detector allows us to measure the momentum of the recoiling spectator proton down to about 70 MeV/c. This momentum measurement constrains the initial four-momentum of the scattered neutron in the reaction $D(e, e'p_s)X$ and, hence, enables us to select almost free neutrons.

We propose to use this technique to extract the structure function F_2^n at x from 0.1 up to 0.8 over a significant range in Q^2 (from about 1 to 14 GeV$^2/c^2$) and W from the nucleon mass, M, to 4.5 GeV with a beam energy of 11 GeV. CLAS12 will be used in its standard configuration with luminosities up to $5 \cdot 10^{33}$ cm^{-2}s^{-1}. We request a total of 40 days of new beamtime in Hall B (35 days at 11 GeV for the measurement and five days of 11 GeV and lower energies for background studies and calibration runs).

Contents

1 Technical Participation of Research Groups **3**
1.1 Old Dominion University . . . 3
1.2 Hampton University . . . 3
1.3 James Madison University . . . 3
1.4 The College of William and Mary . . . 4

2 Introduction **5**

3 Physics Motivation and Theoretical Background **6**
3.1 Nucleon Structure at Large x . . . 7
3.2 Quark-Hadron Duality for the Neutron . . . 8
3.3 Large x-Parton Distribution Functions . . . 10
3.4 Neutron Elastic Scattering . . . 10
3.5 Other Physics Topics Accessible with BONUS . . . 12
3.5.1 Semi-Inclusive Meson Production . . . 12
3.5.2 Measuring the Meson Cloud . . . 13
3.5.3 Other Target Materials . . . 14

4 Tagged Structure Functions **14**
4.1 Spectator Tagging . . . 14
4.2 Backgrounds . . . 16
4.2.1 Target Fragmentation . . . 16
4.2.2 Off-Shell Corrections . . . 16
4.2.3 Final State Interactions . . . 22

5 Experimental Setup and Recoil Detector **25**
5.1 Deuterium Target . . . 26
5.2 Central Detector Solenoid . . . 26
5.3 Radial Time Projection Chamber . . . 26
5.4 Custom Gas Electron Multipliers . . . 28
5.5 Readout Electronics . . . 29
5.6 Some First Results from 2005 Run . . . 30

6 Expected Results **30**
6.1 Monte Carlo Simulation . . . 30
6.2 Resolution . . . 34
6.3 Background Events . . . 34
6.4 Systematic Errors . . . 36
6.4.1 Sensitivity of F_2 Extraction on $R = \sigma_L/\sigma_T$ . . . 37
6.5 Expected Accuracy . . . 39
6.6 Upgrade Possibilities for the RTPC . . . 44

7 Summary and Beam Time Request **46**

1 Technical Participation of Research Groups

1.1 Old Dominion University

The Old Dominion University group is actively involved in this proposal, as well as several other proposal using CLAS12. Other members of our group are also pursuing a proposal for Hall A, but their contributions are not included here.

Among CLAS12 baseline equipment, the group intends to take responsibility for the design, prototyping, construction and testing of the Region 1 Drift Chamber. Five faculty (including one research faculty) and one technician are likely to work at least part time on this project in the next few years. Funding for the group is from DOE and from the university (75% of research faculty salary + one regular faculty summer salary + 50% of the technician).

The university has also provided 6,000 square feet of high bay laboratory space with clean room capabilities for our use. We will seek other sources of funding as appropriate. Gail Dodge is the chair of the CLAS12 Steering Committee and the user coordinator for the CLAS12 tracking technical working group.

Beyond the baseline equipment, the group is also interested in exploring improvements to the BONUS detector and a future RICH detector for CLAS12.

1.2 Hampton University

Hampton University (HU) is actively involved in this proposal, as well as in the original BONUS experiment. The group is also heavily involved in Hall C, where commitments have been made to build base equipment.

The HU group will continue to support development, augmentation, and use of the BONUS target and detector system for 12 GeV in Hall B.

The HU nuclear experimental suite consists of over 1,400 square feet of lab space with an electronic lab station, mechanical lab station, computer/graphic processing bay and a dedicated radiation hot lab. The physics department, furthermore, has a 1,300 square foot class-10,000 clean room for component preparation and module construction.

Research support for the Hampton University nuclear experimental group comes predominantly from the National Science Foundation.

1.3 James Madison University

The James Madison University group is actively involved in this proposal.

Among CLAS12 baseline equipment, the group intends to be involved as a major contributor with the design, prototyping, construction and testing of the pre-shower calorimeter.

Laboratory space is currently being set up at the university for the testing of photomultiplier tubes and fibers.

The group is supported by a grant from the National Science Foundation and has a strong undergraduate research component.

1.4 The College of William and Mary

The College of William and Mary group is actively involved in this proposal, as well as several other proposals using CLAS12. Other members of our group are also pursuing a proposal for Hall A, but their contributions are not included here.

Among CLAS12 baseline equipment, the group is committed to building part of the forward tracking system, but the exact tasks have not yet been determined. At least one faculty member, two graduate students, half a post-doc and several undergraduates are likely to work at least part time on this project in the next few years. Funding for the group is from the DOE and from the NSF. Additional funding will be sought for building the base equipment.

Facilities at William and Mary include a clean room suitable for drift-chamber construction, and, on the time scale of a few years in the future, ample space for detector construction and testing.

2 Introduction

This proposal uses the "spectator tagging" technique to access the structure of the free neutron over a large range of values of Bjorken x, the fraction of the nucleon's momentum carried by the struck quark. It extends the program of structure function measurements from the 5.3 GeV experiment E03-012 (BONUS, or "Barely Off-shell NUcleon Structure", see Ref. [1]) to higher 4-momentum transfers squared, Q^2, and x, in the deep-inelastic scattering region up to $x \approx 0.8$. The method involves detection of low momentum recoil protons with momenta down to 70 MeV/c using the recently built radial time projection chamber (RTPC) as the recoil detector, in coincidence with high–energy electron scattering.

The proposed experiment will study the structure of free neutrons with comparable detail and precision as has been achieved for the proton at the highest possible x values. For this goal, we will use the BONUS recoil detector and a thin deuterium target to "tag" scattering events on a nearly on-shell, loosely bound neutron by detecting slow protons emitted in the backward direction relative to the momentum transfer vector. Many other experiments will be possible with this apparatus, using other nuclear targets and/or detection of other nuclear fragments, exploring topics from the high–momentum structure of light nuclei to coherent production of mesons.

Structure functions of the nucleon reflect the defining features of QCD: asymptotic freedom at large momenta and small distance scales, as well as confinement and non-perturbative effects at the hadronic scale. From measurements of these structure functions in the scaling region, one can infer the momentum and spin carried by the quarks and (via perturbative evolution) the gluons inside the nucleon. At the same time, through scaling violations and $1/Q^2$ power corrections to the leading-twist structure functions, one gains access to the quark-gluon dynamics in a bound hadronic system.

After more than three decades of measurements at many laboratories worldwide, an impressive amount of data have been collected, extending over several orders of magnitude in x and Q^2. However, there are still regions of the kinematic phase space where data are scarce or imprecise. A significant step towards filling the gaps was made by the BONUS experiment E03-012 at 5.3 GeV, which measured the structure function of a nearly free neutron in the deep-inelastic region up to $x = 0.56$, at $Q^2 = 4$ (GeV/c)^2, and through the resonance region at higher x. Due to the lower energy available, E03-012 was not able to penetrate far into the deep-inelastic region. Jefferson Lab with an 11 GeV beam energy will for the first time allow one to reach values of x as high as $x \approx 0.85$ for $W > 1.8$ GeV and $x \approx 0.8$ in the deep-inelastic region above $W > 2$ GeV.

One of the most interesting open questions about the behavior of the structure functions is what happens at the extreme kinematic limit $x \to 1$, where nearly all of the nucleon momentum is carried by a single quark. This limit is dominated by the relative contributions of the u and d valence quarks. Simple phenomenological models like the SU(6) symmetric quark model predict significantly different behavior than perturbative QCD or quark models with improved hyperfine interactions. One can study this region via the ratio of the neutron and proton unpolarized structure functions F_2^n/F_2^p. Although F_2^p is well-known, the traditional way of extracting F_2^n has been with the use of nuclear targets, which for inclusive experiments requires models for the nuclear physics and a subtraction of the F_2^p background.

Another interesting question is whether Bloom-Gilman duality holds as well for the neu-

tron as it does for the proton. The beautiful data for F_2^p in the resonance region show remarkable agreement with extrapolations of the deep-inelastic results to lower Q^2 at comparable x, when one averages over the resonance peaks. While data in the resonance region have been collected in experiment E03-012, corresponding data in the deep-inelastic region have not been available. The new data with the 11 GeV beam will allow, for the first time, duality in the neutron structure function to be extensively tested. Finally, measurements of elastic scattering cross sections on the neutron are needed to gain additional information on its form factors at high Q^2, in a largely independent and complementary approach to the existing Jefferson Lab experiments.

In this Proposal to the Jefferson Lab Program Advisory Committee, we focus on measurements of the inclusive neutron structure functions at high x, including the resonance and elastic region, with detection of a slow backward–going spectator proton. We concentrate on inclusive scattering of 11 GeV electrons; however, many semi-inclusive and exclusive channels (*e.g.*, pion production) can be studied at the same time with this technique. Future extensions to lower or higher beam energy or other final states are possible.

The proposal extends the 5.3 GeV BONUS experiment E03-012, which demonstrated the principle of slow proton tagging, taking data on the nearly free neutron structure function up to $x \simeq 0.6$. It will complete the program of large-x measurements of the neutron structure function in the deep-inelastic region. In the following, we explain the theoretical motivation and experimental method in more detail. We then describe the target–detector system with a first look at some results of experiment E03-012 and then show the results from our simulations with expected results. We conclude with a summary and our beam time request to the PAC.

3 Physics Motivation and Theoretical Background

Most of our information on the structure of the nucleon — from its elastic form factors, to its deep inelastic structure functions — comes from many decades of experiments on proton targets. A complete determination of the valence content of the nucleon can be achieved only when both its u and d quark distributions are known, which necessarily requires information on the structure of the neutron. The absence of free neutron targets has meant that the traditional method for extracting neutron structure information has been to use deuterium targets, and apply nuclear corrections arising from the Fermi motion and binding of the nucleons in the deuteron. While this is sufficient in some cases, for many neutron observables, especially ones sensitive to the high momentum components of the deuteron wave function, the nuclear model uncertainties can be rather large. As a result, our knowledge of the structure of the neutron, especially in the deep inelastic region at large x, is inadequate. Given the extremely high quality of proton data that are being accumulated at Jefferson Lab and other facilities, obtaining a similar level of accuracy for the structure of the free neutron is a high priority.

In this section we highlight several examples which would benefit dramatically from a more accurate determination of the structure of the free neutron. We focus on the ratio of d to u quark distributions at large x, which currently has very large (over $\sim 50-100\%$) uncertainties for $x > 0.6$. Other quantities which will be able to be measured with the proposed

setup include the elastic neutron form factor, quark-hadron duality, large-x parton distribution functions, semi-inclusive DIS channels, hard exclusive reactions such as deeply-virtual Compton scattering or deeply-virtual meson-production, as well as the inclusive structure function of a virtual pion.

3.1 Nucleon Structure at Large x

Although a large body of deep inelastic structure function data exists over a wide range of x and Q^2, the region $x > 0.6$ is not well explored. For $x \geq 0.4$ the contributions from the $q\bar{q}$ sea are negligible, and the structure functions are dominated by the valence quarks.

Knowledge of the valence quark distributions of the nucleon at large x is vital for several reasons. The simplest SU(6) symmetric quark model predicts that the ratio of d to u quark distributions in the proton is 1/2, however, the breaking of this symmetry in nature results in a much smaller ratio. Various mechanisms have been invoked to explain why the $d(x)$ distribution is softer than $u(x)$. If the interaction between quarks that are spectators to the deep inelastic collision is dominated by one-gluon exchange, for instance, the d quark distribution will be suppressed, and the d/u ratio will tend to zero in the limit $x \to 1$ [2]. This assumption has been built into most global analyses of parton distribution functions [3], and has never been tested independently. On the other hand, if the dominant reaction mechanism involves deep inelastic scattering from a quark with the same spin orientation as the nucleon, as predicted by perturbative QCD counting rules, then the effect is to perturb the spin-flavor symmetric wave function such that d/u tends to $\approx 1/5$ as $x \to 1$ [4]. Determining d/u experimentally would therefore lead to important insights into the mechanisms responsible for spin-flavor symmetry breaking.

Because of the 4:1 weighting of the squared quark charges between the up and down quarks, data on the proton structure function, F_2^p, provide strong constraints on the u quark distribution at large x,

$$F_2^p(x) \;=\; x \sum_q e_q^2 \left(q(x) + \bar{q}(x)\right) \;\approx\; x\left(\frac{4}{9}u(x) + \frac{1}{9}d(x)\right) \;. \tag{1}$$

The determination of the d quark distribution, on the other hand, requires in addition the measurement of the neutron structure function, F_2^n. In particular, the d/u ratio can be determined (at leading order in α_s) from the ratio of neutron to proton structure functions,

$$\frac{F_2^n}{F_2^p} \;\approx\; \frac{1 + 4d/u}{4 + d/u} \;, \tag{2}$$

provided $x \geq 0.4$ (at a moderate to high Q^2) so that sea quark content can be neglected. These kinematics are ideal for measurements at Jefferson Lab with an 11 GeV electron beam energy.

In the past, data on F_2^n have been extracted primarily from inclusive scattering off deuterium. Unfortunately, theoretical uncertainties in the treatment of nuclear corrections have led to ambiguities in the extracted F_2^n at large x. In particular, inclusion of Fermi motion and nucleon off-shell corrections in the deuteron can lead to values for F_2^n/F_2^p which differ by 50% already at $x = 0.75$, and by a factor 2–3 at $x = 0.85$ [6, 7, 8, 9]. This uncertainty

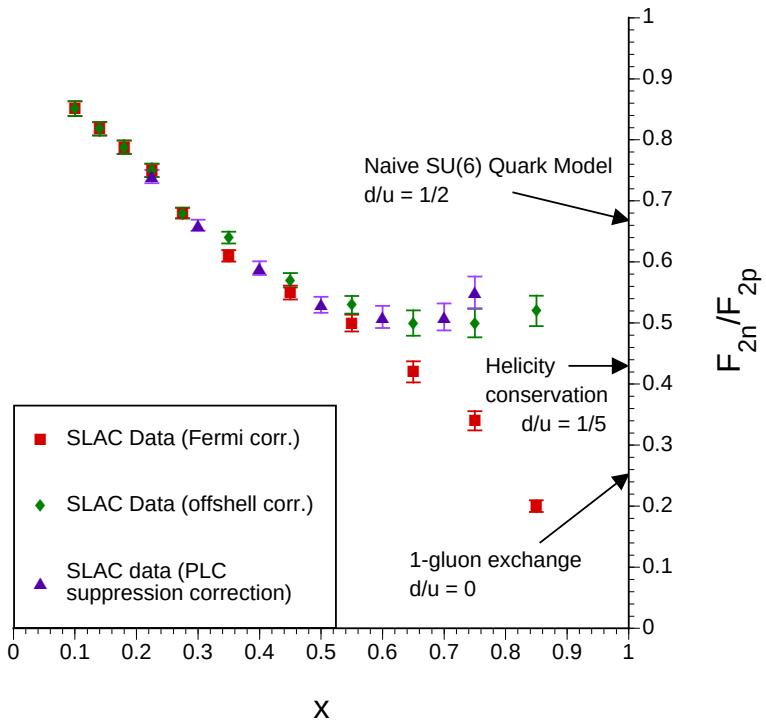

Figure 1: Neutron to proton structure function ratio, extracted from SLAC proton and deuteron data [6], assuming different prescriptions for the nuclear corrections, as described in the text. Several theoretical predictions for the $x \to 1$ limits are indicated by arrows.

is illustrated in Fig. 1, which shows F_2^n/F_2^p extracted from the same SLAC data on the proton and deuteron structure functions [6], with the nuclear corrections estimated on the basis of Fermi motion only (squares), taking nucleon off-shell effects into account [7, 9] (diamonds), and a model assuming suppression of point-like configurations (PLC) in the bound nucleon [9] (triangles). The nuclear model dependence is as large or larger than the spread in the model predictions for the $x \to 1$ behavior, which are indicated by the arrows. The tagged structure function method for measuring F_2^n proposed here virtually eliminates the uncertainties from nuclear models.

3.2 Quark-Hadron Duality for the Neutron

Measurements [10, 11] at Jefferson Lab of the unpolarized structure functions on hydrogen, deuterium and nuclei in the resonance region have established to high accuracy the remarkable phenomenon of Bloom-Gilman duality down to $Q^2 \sim 1$ (GeV/c)^2 or even lower. Also, HERMES has observed duality in the proton spin asymmetry A_1 [12], and JLab data are being analyzed to test duality in both the spin-dependent proton g_1^p and neutron g_1^n structure functions. The recently approved MINERvA experiment at Fermilab will investigate duality in neutrino scattering as well.

Quark-hadron duality here refers to the observation that the structure functions in the resonance region at low W and Q^2 show a striking similarity, when averaged over resonances, to the scaling structure functions measured in the deep inelastic region at high W and Q^2.

This phenomenon is even more remarkable given that the resonance–scaling duality appears to hold in each of the prominent resonance regions separately, indicating the presence of duality on a rather local level. While a global version of duality, with integration over many resonances, can be qualitatively understood in the context of the twist expansion in QCD, at present the origin of local duality is unclear and the subject of considerable theoretical interest [13, 14, 15].

The appearance of duality in QCD is usually taken to indicate that the size of higher twist contributions to structure functions, involving long-range correlations between quarks and gluons, is small [16]. As discussed by Close and Isgur [14], the higher twist effects are responsible for the difference between the scaling structure function expressed in terms of an incoherent sum of the squares of quark charges,

$$F_2(x) \;=\; x \sum_q e_q^2 \; q(x) \;, \tag{3}$$

and that given in terms of squares of form factors,

$$F_1 \;=\; M^2 \left(|G_+|^2 + |G_-|^2 \right) \delta(W^2 - M_{N^*}^2) \qquad \text{and} \tag{4}$$

$$F_2 \;=\; (1+\nu^2/Q^2)^{-1} M\nu \left(|G_+|^2 + 2|G_0|^2 + |G_-|^2 \right) \delta(W^2 - M_{N^*}^2) \;, \tag{5}$$

involving a coherent sum over individual quark flavors,

$$|G_m|^2 \;=\; \left| \sum_q e_q \; G_m^{(q)} \right|^2 \;. \tag{6}$$

Here the helicity amplitudes $G_m (m = \pm 1, 0)$ are defined in terms of $N \to N^*$ transition matrix elements:

$$G_m \;\propto\; \langle N^*, \lambda' = m - 1/2 | \epsilon_m^\mu \cdot j_\mu(0) | N, \lambda = 1/2 \rangle \;, \tag{7}$$

with λ (λ') the helicity of the initial (final) state, ϵ_m^μ the photon polarization vector, and j_μ the electromagnetic current.

In the flavor-symmetric limit, the difference between these dual descriptions, which represents violations of Bloom-Gilman duality, is precisely due to the presence of higher twist effects. Diagrammatically these can be represented as off-diagonal quark transitions, in which the photon scatters from the nucleon with strength proportional to $\sum_{q \neq q'} e_q e_{q'}$. The experimental verification of Bloom-Gilman duality for the proton [17] implies that the single-quark scattering mechanism dominates the interaction above $Q^2 \sim 0.5$ (GeV/c)^2.

On the other hand, it has been observed that for the specific case of the proton, the sum over the off-diagonal contributions $\sum_{q \neq q'} e_q^{(p)} e_{q'}^{(p)} = 0$ simply because of the quark charge assignments in the proton [14]. This leaves open the possibility that duality for the proton may not necessarily be an indication of suppression of higher twist effects, but merely the result of a fortuitous cancellation of their coefficients. For the neutron, however, there is no such cancellation, since $\sum_{q \neq q'} e_q^{(n)} e_{q'}^{(n)} \neq 0$. Furthermore, within a simple harmonic oscillator quark model, Close and Isgur [14] find that the neutron structure functions should exhibit systematic deviations from local duality, and that duality should occur at higher W

for the neutron than for the proton. These arguments can be further refined by considering more sophisticated quark models, including various mechanisms of SU(6) symmetry breaking [18]. The true origins of Bloom-Gilman duality in the nucleon can be determined with the verification of this phenomenon in the neutron.

In the earlier BONUS experiment at 5.3 GeV, the structure function of the neutron was measured in the nucleon resonance region, at $W < 2$ GeV, over a range of x and Q^2. To test duality, one requires data at the same x but at higher Q^2, in the deep-inelastic region, $W > 2$ GeV. This experiment will therefore provide the vital missing information which will enable the workings of duality for the neutron to be tested for the first time at the same level as for the proton.

3.3 Large x-Parton Distribution Functions

Parton distribution functions (PDFs) give the probability to find partons in a hadron as a function of the fraction x of the nucleon's momentum carried by the parton. Parton distributions are determined from experimental results generally on short distance scattering of the partons, typically from global fits to a wide range of processes and data - such as deep inelastic scattering. Precise knowledge of the nucleon's flavor structure and precision tests on the evolution of leading twist parton densities as predicted by QCD are key questions of present day studies of structure functions. Such flavor decomposition requires first, however (a) separation of the flavor non-singlet and singlet evolution; and (b) precision knowledge of u_v and d_v in the entire x-range - if possible with the same accuracy. One of the most fundamental properties of the nucleon is the structure if its valence quark distributions, and the down valence quarks can be best measured off neutrons.

Although the PDFs are generally well determined in the small and medium x-ranges, it has been shown that their uncertainty grows rapidly for $x > 0.1$. In the past few years there has been considerable progress towards understanding some of the uncertainties in the individual measurements that contribute to our knowledge of the large x parton distributions, but in some cases this has led to an increase in the uncertainty of the large x PDFs rather than a reduction[5]. Fig. 2 shows the uncertainties in the CTEQ6 up and down quark distributions. The substantial uncertainty on the down quark distribution at large x is due largely to the lack of available data, and the substantial uncertainties associated with neutron data extrapolated from deuteron measurements.

The BONUS neutron structure function data at large x will be included in global PDF fitting efforts, such as CTEQ, to reduce these uncertainty bands. CTEQ is currently investigating a duality-based approach to utilize the 5.3 GeV BONUS data.

We mention, additionally, that reliable knowledge of parton distributions at large x is crucial to many searches for new physics signals beyond the standard model in the next generation of collider experiments [5].

3.4 Neutron Elastic Scattering

The elastic form factors of the nucleon are the most basic observables which reflect its composite nature. As with the deep inelastic structure functions, a considerable body of data now exists on the elastic electric and magnetic form factors of the proton, while the

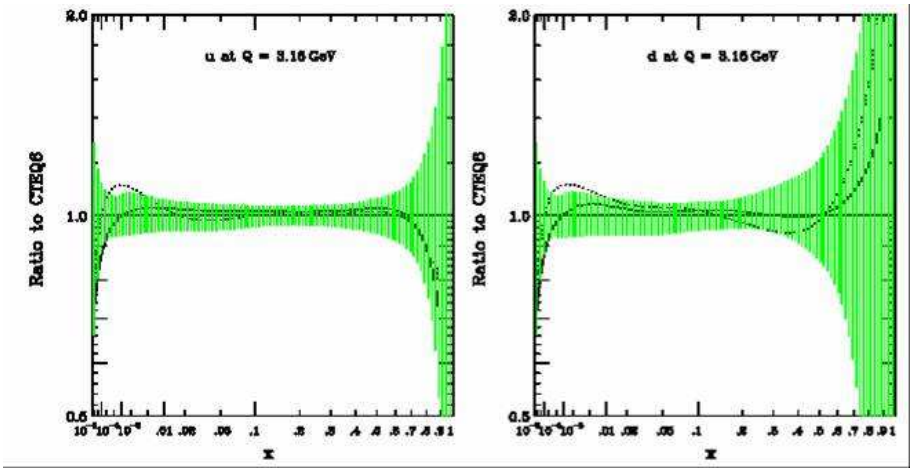

Figure 2: Uncertainty bands for the u and d quark distribution functions at $Q^2 = 10\,\mathrm{GeV}^2/c^2$. The solid line is CTEQ5M1 and the dotted is MRST2001.

analogous form factors of the neutron are known much less accurately and over a more limited range of kinematics.

The magnetic form factor of the proton is reasonably well determined to $Q^2 = 30\,(\mathrm{GeV}/c)^2$. Accurate measurements of the neutron magnetic form factor, $G_M^n(Q^2)$, currently extend to $Q^2 \approx 5\,(\mathrm{GeV}/c)^2$ (E94-017 [19, 20]), with plans to measure $G_M^n(Q^2)$ to $Q^2 \approx 14\,(\mathrm{GeV}/c)^2$ with the upgraded CLAS12 detector at a 12 GeV CEBAF [19]. These experiments involve quasi-elastic scattering from the deuteron, with measurement of the ratio of scattered neutron to proton events to determine G_M^n/G_M^p. Unfortunately, quasi-elastic measurements at high Q^2 require more elaborate treatments of nuclear corrections, including the effects of relativity, final state interactions, and possible non-nucleonic degrees of freedom.

The recent experiments at MAMI, Bates and JLab measuring double spin asymmetries in quasi–elastic scattering off deuteron and ^{3}He targets allow a nearly model–independent extraction of the *ratio* G_E^n/G_M^n, up to Q^2 of about $1.5\,(\mathrm{GeV}/c)^2$. In future experiments, this method will be extended to even higher Q^2. However, to extract absolute values of either G_E^n or G_M^n, one needs to measure cross sections. The availability of a nearly free neutron target for cross section measurements will enable one to measure different combinations of G_E^n and G_M^n at unprecedented high Q^2, essentially free from uncertainties from nuclear effects as well as neutron detection efficiencies.

Experiment E94-017 extracted the magnetic form factor of the neutron, G_M^n, from a measurement of the cross section ratio, R_D, of quasi-elastic electron-neutron and electron-proton scattering on a deuterium target, which is nearly equal to the free nucleon e-n to e-p cross section ratio

$$R_D = a(Q^2)\,\frac{\frac{(G_E^n)^2+\tau\,(G_M^n)^2}{1+\tau} + 2\,\tau\,(G_M^n)^2\,\tan^2(\Theta/2)}{\frac{(G_E^p)^2+\tau\,(G_M^p)^2}{1+\tau} + 2\,\tau\,(G_M^p)^2\,\tan^2(\Theta/2)}\,,$$

with $\tau = \frac{Q^2}{4\,M^2}$. Details can be found in [20]. This ratio method also requires information on the proton elastic scattering cross section and G_E^n. The total proton elastic cross section has been well measured and, while the uncertainties on G_E^n are large, G_E^n is small compared

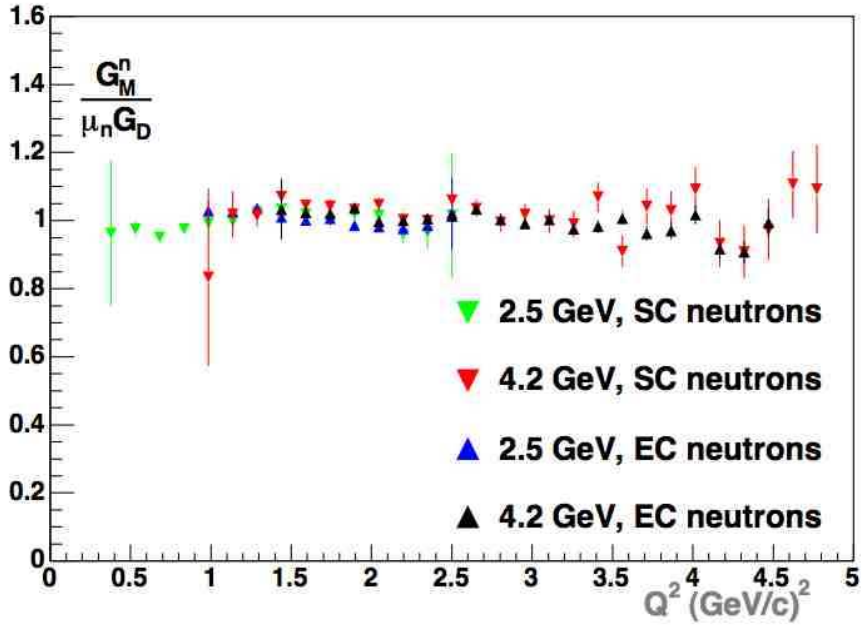

Figure 3: The magnetic form factor of the neutron normalized by the dipole form factor as a function of Q^2 from experiment E94-017 [20].

to the other form factors, and its contribution to the value of the ratio diminishes as Q^2 becomes larger. The result from experiment E94-017 is shown in Fig. 3.

The neutron form factor G_M^n measurements will be extended up to $Q^2 = 14$ GeV$^2/c^2$ with a dedicated CLAS12 experiment. Our proposal can cross-check those results with an indepedent measurement that does not rely on neutron detection efficiency.

3.5 Other Physics Topics Accessible with BONUS

The following physics topics are also of high current interest, and will become accessible with the same recoil detection technology used for BONUS. However, at present not all of the necessary equipment or calculations are in hand, so a full exposition will have to await separate dedicated proposals.

3.5.1 Semi-Inclusive Meson Production

Production of mesons in the current fragmentation region of semi-inclusive deep-inelastic scattering from nucleons is an important method of isolating different flavors of partons. Detecting positively or negatively charged pions, for instance, off the proton at large x and large $z = E_\pi/\nu$ preferentially selects u and d quarks, respectively. While semi-inclusive DIS data are rapidly accumulating in electron scattering from protons, no semi-inclusive data exist for neutron targets.

A natural extension of the BONUS technique in inclusive DIS off the neutron is to consider *semi-inclusive* DIS from a nearly-free neutron in the deuteron. Availability of semi-inclusive neutron data will greatly complement our ability to perform flavor separation of

parton distribution functions. In addition to pions, observation of a K^+ as the leading meson produced in the current fragmentation region would imply scattering from either a u or $\bar{s}$ quark. Since isospin symmetry implies that $\bar{s}^p = \bar{s}^n$ (and $u^p = d^n$), by detecting K^+ mesons off the proton or neutron, one would be sensitive to the u or d quark distribution in the proton, respectively. Other examples of the benefits of having neutron targets for semi-inclusive DIS include access to flavor asymmetries of the proton sea, $\bar{d} - \bar{u}$, as well as possible tests of isospin symmetry breaking itself in parton distributions.

3.5.2 Measuring the Meson Cloud

In the early 1970s, Sullivan [21] pointed out that electron Deep Inelastic Scattering (DIS) off a proton target includes a contribution originating from scattering off the meson cloud of the nucleon, as shown in Fig. 4. This so-called Sullivan process was shown to persist even at large Q^2 scales. An immediate consequence of the Sullivan process is that the nucleon parton distributions contain a component which can be attributed to the meson cloud. In the early 1980s, Thomas [22] predicted several implications of the Sullivan process for nucleon parton distributions using a cloudy-bag model for describing the meson cloud. In particular, it was predicted that the nucleon sea should have an up/down sea-quark flavor asymmetry, as well as an $s/\bar{s}$ asymmetry for the strange quark sea. Support for an up/down sea-quark

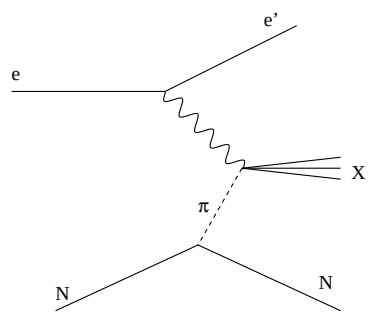

Figure 4: The Sullivan process.

flavor asymmetry was initially provided in the early 1990's by the NMC collaboration's measurement [23] of violation of the the Gottfried Sum Rule. Independent confirmation of the $\bar{d}/\bar{u}$ flavor asymmetry was later provided by Drell-Yan experiments [25, 26, 27, 28] and the semi-inclusive DIS measurements at HERMES [29].

The success of the meson-cloud model in explaining the $\bar{d}, \bar{u}$ asymmetry suggests that a direct measurement of the meson cloud in DIS should be feasible. At the HERA e-p collider, meson structure functions were measured in a hard diffractive process, where forward-going neutrons or protons were tagged in coincidence with the DIS events [33].

Measurements of meson structure functions could be done with the BONUS target and detector system using the reactions $p(e, e'p)X$ and $d(e, e'pp)X$. These processes could also contribute a background to the $d(e, e'p)X$ measurement of the neutron structure function in BONUS, if the detected proton was the result of the Sullivan process instead of being the spectator.

To make measurements of the pion structure function using the Sullivan process to provide a pion target in the semi-inclusive reaction $d(e, e'pp)X$, the spectator proton would be detected in BONUS recoil detector and the proton resulting from the pion exchange might

be detected in BONUS detector or in the CLAS12 detector. Preliminary simulations indicate that the protons resulting from pion exchange are dominantly forward-going and have somewhat higher momenta than the spectators.

Measurements of the semi-inclusive reactions $p(e, e'p)X$ and $d(e, e'pp)X$ in BONUS were introduced in a letter of intent submitted to PAC27 [34], which called for a maximum beam energy of 6 GeV. The reviewers expressed concern that at 6 GeV it is not possible for both M_X to be large and $t_{\min}$ to be small, with t the difference between the initial and final four-momentum of the electron. There was also concern that the measurement would be unable to relate to the pion structure function without duality arguments, or that the measurement would be too far from the pion pole for acceptable extrapolation. Further simulation is required to evaluate the feasibility of the measurement with a beam energy of 11 GeV.

Measurements at Jefferson Lab could be a nice complement to those already taken at HERA. The lower beam energy allows access to a higher x region in the pion structure functions at JLab compared to HERA. The large angular and kinematic coverage for the recoiling proton (or proton pair) using the CLAS12 and BONUS detectors would allow a detailed study of the Sullivan process as a function of variables including the recoiling proton momentum and angles. Also, the CLAS12 and BONUS detectors could allow a detection of the $\Lambda \to p\pi^-$ decay, making a measurement of the $p \to K^+\Lambda$ kaon cloud in the nucleon potentially feasible. This could lead to a measurement of kaon structure functions.

3.5.3 Other Target Materials

It has been suggested that the ratio of the mirror nuclei ^{3}He and ^{3}H may be measured to precisely obtain the n/p cross section ratio at large x [35]. The BONUS target could be filled with these gases, and a simple inclusive measurement of this ratio would take substantially less time in CLAS than the direct neutron measurement experiment here proposed since no spectator tagging would be required. Moreover, for reduced theoretical uncertainty, spectator deuterons from the n,p targets in the mirror nuclei could be measured in the BONUS rtpc detector just as the protons are currently. This experiment would have differing theoretical uncertainties, and would provide a nice complement to the BONUS result. However, issues associated with a ^{3}H target still need to be investigated.

4 Tagged Structure Functions

4.1 Spectator Tagging

The measurement of tagged structure functions in semi-inclusive deep inelastic scattering (DIS) from the deuteron with a slow recoil proton detected in the backward hemisphere, $e + D \to e + p + X$, allows the resolution of the ambiguities introduced by nuclear model dependence for deep-inelastic, as well as (quasi-)elastic, scattering [36, 37, 38]. Within the nuclear impulse approximation, in which the inelastic scattering takes place incoherently from individual nucleons, the differential semi-inclusive cross section can be written as a product of the deuteron spectral function, $\mathcal{S}$, and an effective (bound) neutron structure

function, $F_2^{n(eff)}$ [38]:

$$\frac{d\sigma}{dx dW^2 d\alpha d^2 p_T} \approx \frac{2\alpha_{em}^2(1-\nu/E)}{Q^4}\ \alpha\ \mathcal{S}(\alpha, p_T)\ F_2^{n(eff)}(W^2, p^2, Q^2)\ . \tag{8}$$

(For the full expression for the differential cross section in terms of the transverse and longitudinal structure functions see Ref. [38].) Here $W^2 = (p_d + q - p_s)^2$ is the invariant mass squared of the unobserved hadronic final state, with p_s the momentum of the spectator proton, p_d the momentum of the initial state deuteron, and $p = p_d - p_s$ the momentum of the struck neutron. The variable $\alpha = (E_s - p_s^z)/M$ is the light-cone momentum fraction carried by the spectator proton, and p_T its transverse momentum component (perpendicular to the direction of $\vec{q}$), with $E_s = \sqrt{M^2 + \vec{p}_s^{\,2}}$ the spectator proton energy, and M its mass. The use of the light-cone variable α emphasizes the kinematical dependence of the structure function at high Q^2, since $F_2^{n(eff)}(W^2, p^2, Q^2) \equiv F_2^{n(eff)}(x/(2-\alpha), p_T, Q^2)$. In addition, as discussed in Section 4.2.3 below, the dependence on α is not affected by final state interactions. The pre-factor α in Eq. (8) is related to the so-called "flux-factor" [39]. The degree to which the struck neutron is off-shell is given by

$$M^2 - p^2 \approx 2\vec{p}_s^{\,2} + 2M|\epsilon|\ , \tag{9}$$

where ϵ is the deuteron binding energy. In the limit $p^2 \to M^2$ (and $\alpha \to 1$), the effective neutron structure function $F_2^{n(eff)}(W^2, Q^2, p^2) \to F_2^n(W^2, Q^2, M^2) \equiv F_2^n(x, Q^2)$, the free neutron structure function. The p^2 dependence of $F_2^{n(eff)}$ depends somewhat on the theoretical assumptions made about the off-shell behavior of the photon–bound nucleon scattering amplitude. To avoid these uncertainties one therefore needs to minimize the degree to which the struck neutron is off-shell, by restricting oneself to small values of the spectator proton momentum, p_s. At the low momenta proposed in this experiment the uncertainty associated with the choice of deuteron wave function (or the spectral function, $\mathcal{S}$) is also expected to be quite small.

The calculation of the kinematic variables for the experiment will be done in a covariant way, taking into account the four-momentum vector of the on-shell spectator proton for the calculation of the electron-neutron scattering. The Bjorken scaling variable $x = \frac{Q^2}{2M\nu}$ then becomes

$$x^\star = \frac{Q^2}{2\, p^\mu\, q^\mu} = \frac{Q^2}{2\left((M_d - E_s)\,\nu + \vec{q}\ \cdot\ \vec{p}_s\right)} \tag{10}$$

where $q^\mu = (\nu, \vec{q})$ is the momentum transfer 4-vector, $p^\mu = (M_d - E_s, -\vec{p}_s)$ is the momentum 4-vector of the off-shell neutron, and M_d is the mass of the deuterium nucleus. In a covariant description the struck nucleon is on its energy shell, but off its mass shell. The mass of the free nucleon M is therefore replaced with the off-shell mass of the bound nucleon:

$$M^{\star 2} = (M_d - E_s)^2 - \vec{p}_s^{\,2}. \tag{11}$$

The invariant mass of the final hadronic state in $d(e, e'p_s)X$ scattering can be expressed as:

$$W^{*2} = (p^\mu + q^\mu)^2 = (M_d - E_s + \nu)^2 - (\vec{q} - \vec{p}_s)^2\ . \tag{12}$$

4.2 Backgrounds

The choice of backward kinematics for the spectator proton serves to minimize effects from final state interactions, as well as independent target fragmentation, while the restriction to small proton momenta mostly eliminates uncertainties associated with the deuteron wave function and on-shell extrapolation. In this section we consider each of these corrections to the impulse approximation in Eq. (8) explicitly. Corrections to the impulse approximation from the breaking of the factorization in Eq. (8) were analyzed in Ref. [40] for the inclusive deuteron structure function, and found to be quite small ($\leq 1\%$) for the kinematics considered here. The total estimated errors to F_2^n resulting from these corrections are given in Section 6.

4.2.1 Target Fragmentation

The production of low momentum protons originating from the hadronic debris of the struck neutron is minimized by enforcing a large rapidity gap between the recoil proton and the rest of the hadronic debris [37, 41]. While in the forward hemisphere (current fragmentation region) there are potentially large contributions from direct quark→proton fragmentation, especially at low x, in the backward hemisphere (target fragmentation) these will be strongly suppressed. The direct fragmentation contribution is also expected to decrease with decreasing spectator proton momentum.

Non-spectator protons can be produced in coincidence with DIS electrons through several processes, none of which contributes significantly to the spectrum of *backward-moving* protons. First of all, protons in the current quark fragmentation region will be exceedingly rare in our kinematics (because of the high W needed to produce a baryon-antibaryon pair) and will be going forward with respect to $\vec{q}$. Secondly, protons could come from the target fragmentation when either a neutron or a proton is struck by the virtual photon.

The Sullivan process described earlier can be considered as part of this signal. However, one can prove rigorously that no such proton can be moving backward either in the lab or relative to $\vec{q}$ if the initial struck nucleon was at rest. For instance, a preliminary simulation of the Sullivan process scattering in the BONUS kinematics indicates that the protons resulting from the two processes, $e\ n \rightarrow e'\ p\ X$ (where $n \rightarrow \pi^-\ p$) and $e\ p \rightarrow e'\ p\ X$ (where $p \rightarrow \pi^0\ p$), should be peaked in the forward scattering direction and at higher momenta than the spectator proton. For protons or neutrons moving initially backwards inside the deuteron target, a target fragment moving backwards in the final state is possible but requires large initial backward momentum, which is highly suppressed by the deuteron wave function.

These features are evident from Fig. 5, where the ratio of the plane wave impulse approximation (PWIA), corrected for target fragmentation, to the pure PWIA contribution is shown as a function of the recoil angle, θ_{pq}, of the proton relative to the photon direction. Clearly, the effects of target fragmentation are relevant only in the forward hemisphere, and for $\theta_{pq} > 90°$ are totally negligible, even for large p_s.

4.2.2 Off-Shell Corrections

To minimize theoretical uncertainties associated with extrapolation of the semi-inclusive cross section to the nucleon pole, it is important that the tagged structure functions be

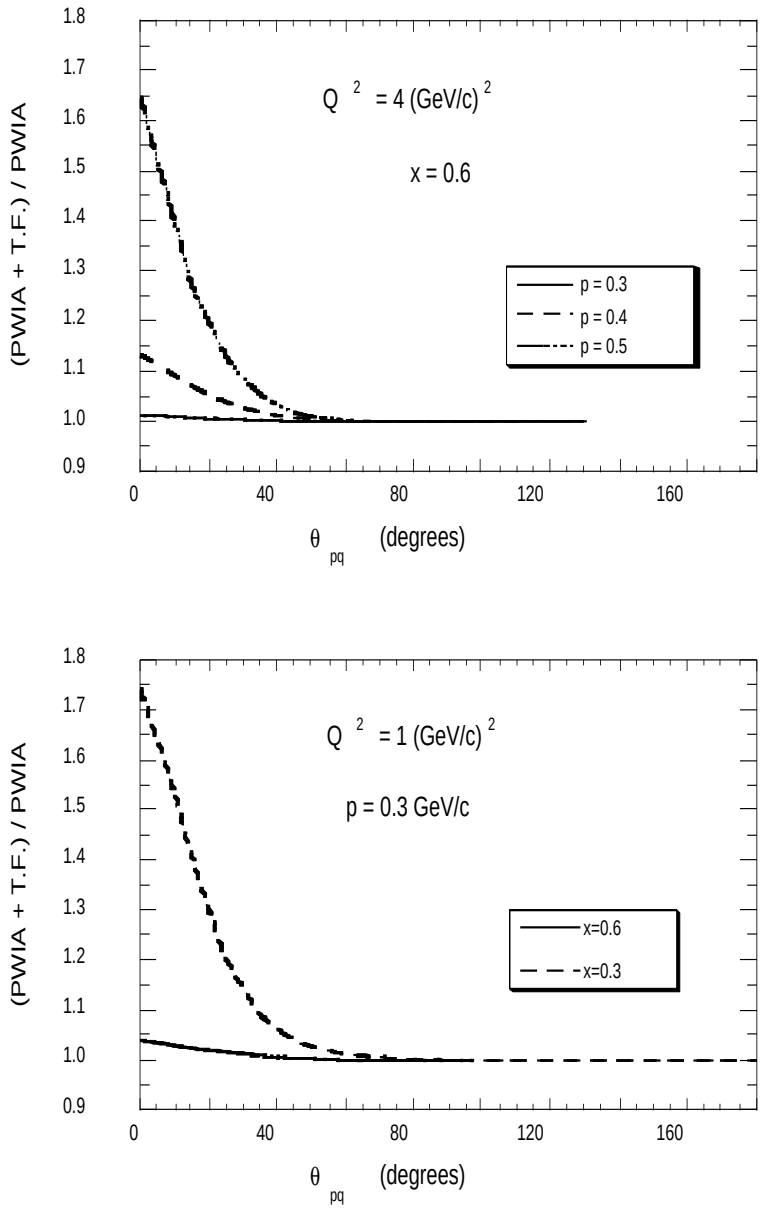

Figure 5: Effect of target fragmentation (TF) on the plane wave impulse approximation (PWIA) calculation of semi-inclusive DIS from the deuteron [37], as a function of the c.m. angle, θ_{pq}, between the spectator proton and the virtual photon.

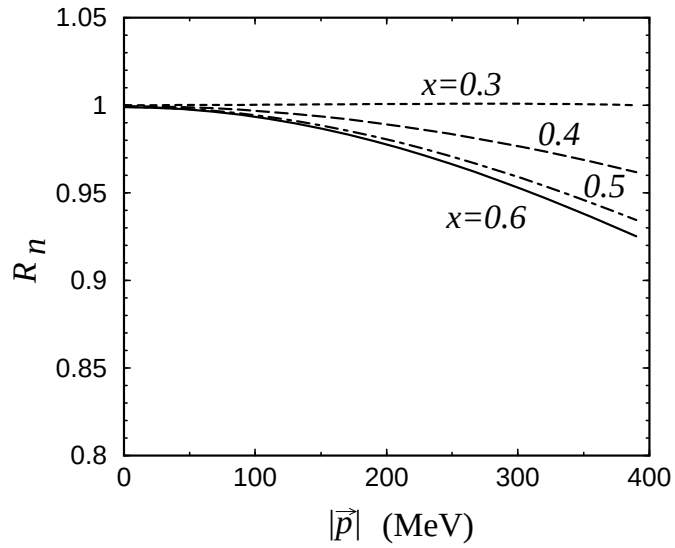

Figure 6: Ratio $R_n \equiv F_2^{n(eff)}(W^2, Q^2, p^2)/F_2^n(W^2, Q^2)$ of the bound to free neutron structure functions, as a function of the spectator proton momentum, in the model of Ref. [40], at $Q^2 = 5$ (GeV/c)^2.

measured for kinematics where the difference $p^2 - M^2$ is as small as possible. To assess the potential model dependence of the extracted neutron structure function on the extrapolation procedure we consider several models based on rather different dynamical assumptions.

In convolution models off-shell corrections appearing at leading twist originate both kinematically, as a consequence of the nucleon's transverse motion in the nucleus, and dynamically, from modifications of the bound nucleon structure. Kinematical off-shell effects can be calculated with very little model dependence, as discussed in Ref. [42], for instance. Dynamical off-shell effects, on the other hand, depend on descriptions of the intrinsic deformation of the bound nucleon structure, and are therefore more model-dependent.

In the covariant spectator model of Ref. [40], the DIS from a bound nucleon is described in terms of relativistic vertex functions which parameterize the nucleon–quark–"diquark" interaction (where "diquark" here refers to a system of a nucleon with one quark removed, which has the quantum numbers of a diquark). The dependence of the vertex functions on the quark momentum and the "diquark" energy is constrained by fitting to the on-shell nucleon (proton) structure function data. The additional dependence of the vertex function on the virtuality of the off-shell neutron is fixed by comparing the calculated deuteron structure function with the inclusive F_2^d data. The resulting ratio $R_n \equiv F_2^{n(eff)}(W^2, Q^2, p^2)/F_2^n(W^2, Q^2)$ of the bound to free neutron structure functions is shown in Fig. 6 as a function of the momentum of the spectator proton, $|\vec{p}_s| = |\vec{p}|$, for several values of x. Not surprisingly, the effect at low $|\vec{p}_s|$ is very small, with the deviation from unity increasing at higher momenta. For $|\vec{p}| \approx 100$ MeV/c the effect is $\leq 1\%$ for $x = 0.6$, where the EMC effect is more pronounced, and essentially zero for $x = 0.3$.

A similar model in which the scattering from an off-shell nucleon is described in terms of a relativistic quark spectral function was introduced in Ref. [42]. In this approach the bound nucleon structure function is evaluated from the free nucleon structure function at a

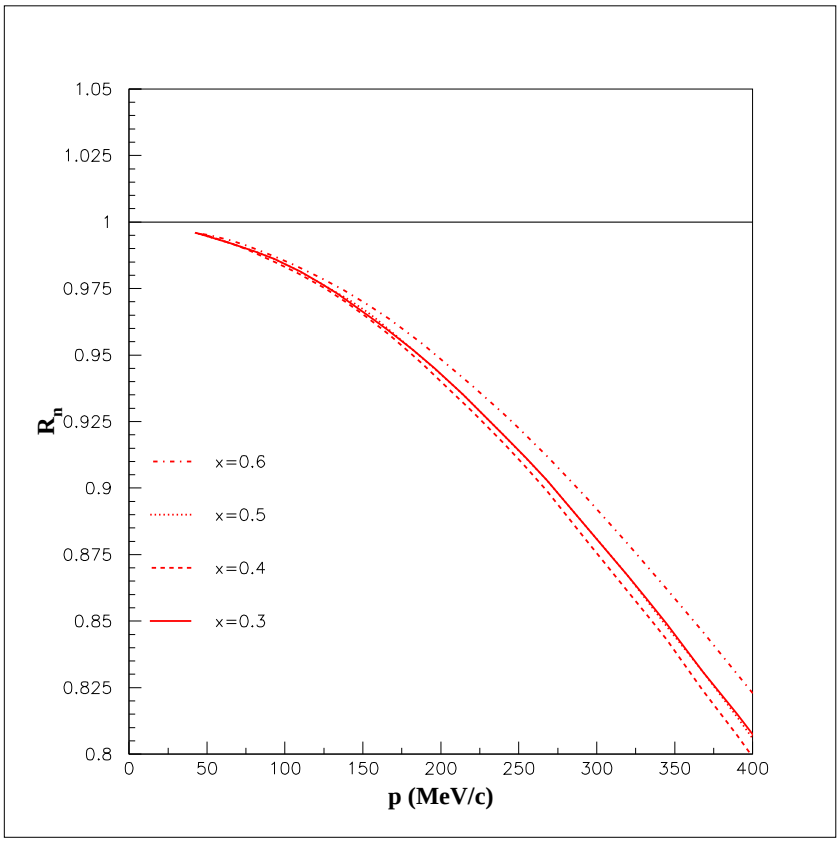

Figure 7: Ratio R_n of the bound to free neutron structure functions, as a function of the spectator proton momentum, in the model of Ref. [42].

shifted value of the quark light-cone momentum fraction, which depends on the mass of the spectator "diquark" system, the bound nucleon momentum, and the binding energy [42]. The resulting ratio R_n of the bound to free neutron structure functions is shown in Fig. 7.

The deviation from unity is again small at low spectator proton momenta, amounting to $\leq 2\%$ for $|\vec{p}_s| \leq 100$ MeV/c, increasing to around 5% for $|\vec{p}_s| = 200$ MeV/c. The results shown are for $Q^2 = 10$ (GeV/c)^2, although the Q^2 dependence is weak. In contrast to Fig. 6, however, the effect in this model is only weakly dependent on x. Similar behavior to that in Figs. 6 and 7 is also observed in the model of Ref. [43], where the assumption of weak binding in the deuteron allows one to calculate the off-shell dependence up to order p^2/M^2. An important constraint on the size of the nucleon's deformation in this approach is provided by the conservation of the number of valence quarks in the bound nucleon,

$$\frac{d}{dp^2} \int_0^1 dx \, q_{val}^{(eff)}(x, Q^2, p^2) = 0 \ , \tag{13}$$

where $q_{val}^{(eff)}$ is the valence quark distribution in the effective nucleon structure function, $F_2^{N(eff)}$. By imposing this constraint, one obtains an overall reduction of the kinematical off-shell effects whose strength can be located either at intermediate values of x, $x \geq 0.4$, as in the models of Refs. [40, 43], or at low values of $x \leq 0.15$, as suggested in Ref. [44].

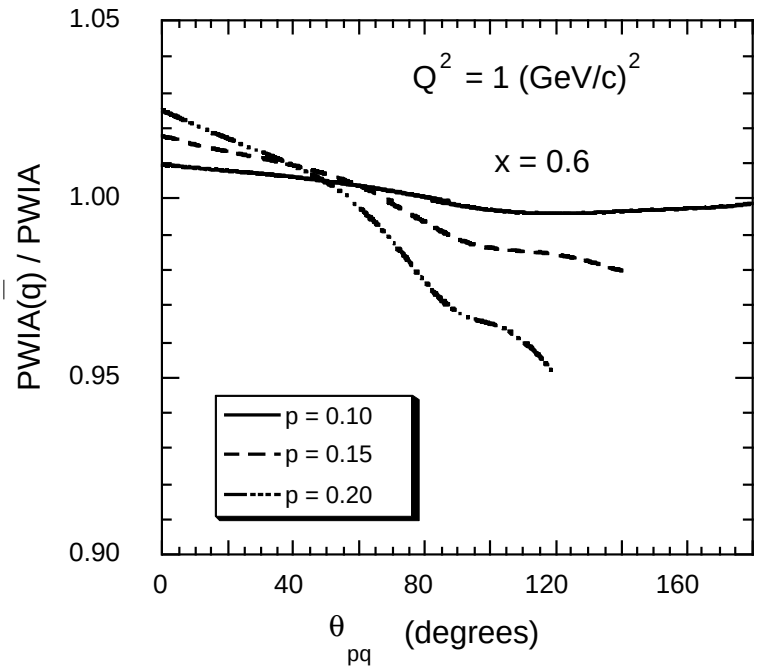

Figure 8: Ratio of bound to free nucleon structure functions, calculated using the model of Ref. [45]. The spectator proton momentum p is in units of GeV/c.

Neglecting the contributions of $N\bar{N}$ pairs to the deuteron wave function, another estimate of the role of nucleon off-shellness can be made simply on the basis of kinematics. In the instant form approach discussed in Ref. [45], the nuclear structure function is related to the free nucleon structure function, evaluated at a shifted energy transfer, $\nu \to \bar{\nu}$, which depends on the degree to which the nucleon is bound (and hence, in the instant form language, off its energy shell). A shifted value of ν corresponds to a shifted value of x and Q^2 at which the nucleon structure function is evaluated. The ratio of the structure functions calculated in the plane wave impulse approximation with the modified variables ("PWIA($\bar{q}$)") to that in which there is no modification is displayed in Fig. 8 as a function of θ_{pq} for $Q^2 = 1$ (GeV/c)^2. Once again, one sees that for low spectator proton momenta, $|\vec{p}_s| \approx 100$ MeV/c, the off-shell modification is less than 1% for all accessible angles. Only when one goes above $|\vec{p}_s| \approx 200$ MeV/c are there any effects at the $\leq 5\%$ level.

While the off-shell modification of the bound nucleon structure function in the above models is weak, the color screening model for the suppression of point-like configurations in bound nucleons [9] predicts somewhat larger deviations from unity of the ratio R_n than that in Figs. 6, 7 and 8. In this model one attributes most or all of the EMC effect to a medium modification of the internal structure of the bound nucleon, and little of the effect to mechanisms such as nuclear binding. On the other hand, since the deviation of the bound to free structure function ratio from the free limit is proportional to $2\vec{p}_s^{\,2} + 2M|\epsilon|$ (Eq. (9)), sampling the data as a function of $\vec{p}_s^{\,2}$ should provide some guidance for a smooth extrapolation to the pole. In practice, considering a momentum interval of 70–200 MeV/c will allow the dependence on p^2 to be constrained. Existing 6 GeV data from the JLab experiment E94-102 (E6) will in addition constrain the behavior of the bound structure

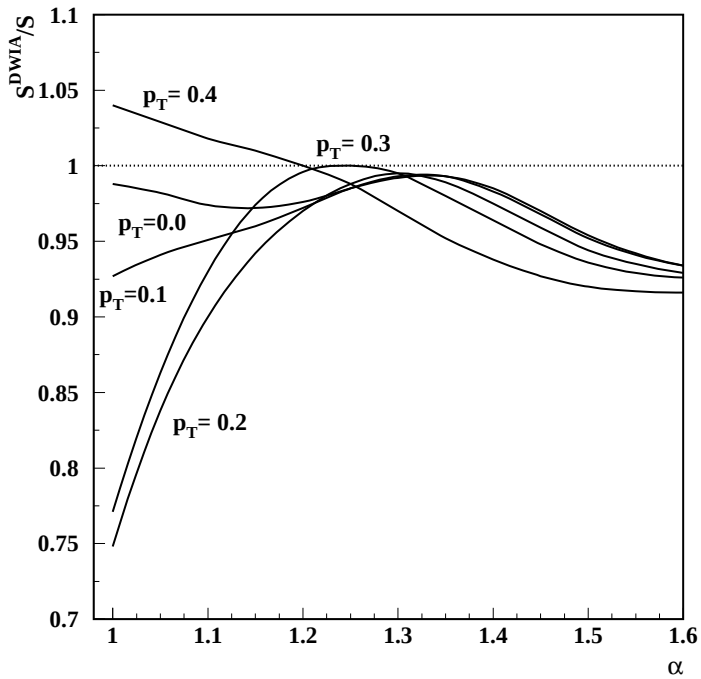

Figure 9: Spectral function calculated with and without FSI effects within the DWIA [38]. The curves correspond to different values of the spectator proton transverse momentum p_T (in GeV/c).

function at larger $|p^2|$ (for spectator momenta between $\approx$ 250 and 700 MeV/c).

Overall, we expect that the extrapolation from the minimum $|\vec{p}_s| \approx 70$ MeV/c, where the bound neutron is only around 7 MeV/c away from its mass-shell, should be relatively free of ambiguities. This is also supported by recent ^{4}He$(\vec{e}, e'\vec{p})$ polarization transfer experiments at Mainz and Jefferson Lab [46] which indicate that the magnitude of the off-shell deformation may be rather small. These experiments measured the ratio of transverse to longitudinal polarization of the ejected protons, which is related to the medium modification of the electric to magnetic elastic form factor ratio.

Using model independent relations derived from quark-hadron duality, one can relate the medium modifications in the form factors to a modification at large x of the deep inelastic structure function of the bound nucleon [47], which suggests an effect of $< 3\%$ for $x \leq 0.8$. The typical momentum of the knocked out protons in the experiments was $\sim$ 50 MeV/c, although the results of the analysis were found not to depend strongly on the proton momentum [47]. These considerations lead us to expect that the extrapolation of the bound neutron structure function to the nucleon pole should introduce minimal uncertainty into the extracted structure function of the free neutron – see also Ref. [48].

4.2.3 Final State Interactions

Another possible source of uncertainty arises from final state interaction (FSI) effects, or rescattering of the spectator proton by the deep inelastic remnants, X, of the scattered neutron. The choice of backward angles is designed to minimize these effects. The magnitude of FSI effects has been estimated in several models, within the framework of the distorted wave impulse approximation (DWIA) [49], and in a string-like model which emphasizes the propagation and hadronization of the partonic debris emanating from the photon–bound nucleon vertex [50]. The strong suppression of FSIs at backward spectator proton angles is evident in both of these calculations.

A direct calculation of the FSI contribution to the cross section requires knowledge of the full dynamics of the spectator proton–X system. In the model of Ref. [49] the effects of FSIs are estimated by comparing with the calculation of FSI effects in the high-energy ^{2}H$(e,e'p)n$ break-up reaction. The effective p–X interaction cross section, σ_{eff}, is approximated [51] by that extracted from soft neutron production in the high-energy DIS of muons from heavy nuclei [52]. The effect of the FSI is then to modify the spectral function $\mathcal{S} \to \mathcal{S}^{DWIA}$ [49], where

$$\mathcal{S}^{DWIA}(\alpha, p_T \approx 0) \sim \mathcal{S}(\alpha, p_T \approx 0) \left[1 - \frac{\sigma_{eff}(Q^2, x)}{8\pi \langle r_{pn}^2 \rangle} \frac{|\psi_d(\alpha, \langle p_T \rangle) \psi_d(\alpha, 0)|}{S(\alpha, p_T \approx 0)/\sqrt{E_s \; E_s(\langle p_T^2 \rangle)}} \right] , \quad (14)$$

with $\langle r_{pn}^2 \rangle$ the average separation of the nucleons within the deuteron, and $E_s(\langle p_T^2 \rangle) = \sqrt{M^2 + p_s^z{}^2 + \langle p_T^2 \rangle}$ the energy evaluated at the average transverse momentum, $\langle p_T^2 \rangle^{1/2} \sim$ 200–300 MeV/c, transferred for the hadronic soft interactions with effective cross section σ_{eff}. The steep momentum dependence of the deuteron wave function, $|\psi_d(\alpha, \langle p_T \rangle)| \ll |\psi_d(\alpha, p_T \approx 0)|$, ensures that FSI effects are suppressed in the extreme backward kinematics.

The effects of FSIs in this model are illustrated in Fig.9, which shows the ratio of the light-cone spectral function including FSI effects within the DWIA to that without [38]. At extreme backward kinematics ($p_T \approx 0$) one sees that FSI effects contribute less than $\sim 5\%$ to the overall uncertainty of the $d(e,e'n)X$ cross section for $\alpha \leq 1.5$. For $p_T = 0.1$ GeV/c the FSI effects are minimized at $\alpha = 1.3$, and remain at the $\leq 5\%$ level for values of α ($\alpha = 1.08$) typical in this experiment.

A more microscopic treatment of the effective rescattering cross section was developed recently in Ref. [50]. Here the FSI due to the propagation of the struck nucleon debris and its hadronization in the nuclear environment was applied to the $A(e,e'(A-1))X$ reaction, in which the residual $(A-1)$ nucleus is detected in coincidence with the scattered lepton. For a deuteron target, this process precisely coincides with that considered here, namely ^{2}H$(e,e'N)X$. The effective cross section, σ_{eff}, describing the interaction of the debris with a nucleon of the $(A-1)$ spectator system in this approach is both time (t) and Q^2 dependent. This result was obtained on the basis of a model [50] which takes into account both the production of hadrons due to the breaking of the color string, which is formed after a quark is knocked out from a bound nucleon, as well as the production of hadrons originating from gluon radiation [53]. The general expression has the form:

$$\sigma_{eff}(t) = \sigma_{tot}^{NN} + \sigma_{tot}^{\pi N} \Big[n_M(t) + n_G(t) \Big] , \quad (15)$$

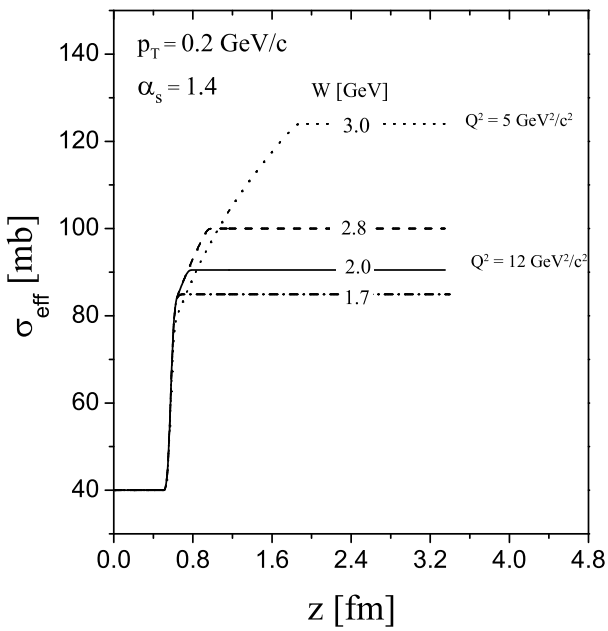

Figure 10: The debris–nucleon effective cross section, σ_{eff}, from Eq. (15) [50], as a function of the longitudinal distance z.

where σ_{tot}^{NN} and $\sigma_{tot}^{\pi N}$ are the total nucleon-nucleon and meson-nucleon scattering cross sections, and $n_M(t)$ and $n_G(t)$ are the effective numbers of created mesons and radiated gluons, respectively. The dependence of σ_{eff} on t (or equivalently on z, the longitudinal distance) and Q^2 or W is illustrated in Fig. 10.

Once the effective cross section of the interaction of the quark debris with the nucleons is defined, the standard eikonal approximation can be used to evaluate the cross section by replacing the struck nucleon momentum distribution with the distorted momentum distribution [54],

$$S^{PWIA}(\vec{p}_s) \to S^{FSI}(\vec{p}_s) = \frac{1}{3}\frac{1}{(2\pi)3}\sum_{\mathcal{M}_d}\left|\int d\vec{r}\ \Psi_{1,\mathcal{M}_d}(\vec{r})S(\vec{r})\chi_f^\dagger\ \exp(-i\vec{p}_s\cdot\vec{r})\right|^2 , \qquad (16)$$

where the relative coordinate $\vec{r} = \vec{b} + z\vec{q}/|\vec{q}|$ is defined in terms of the longitudinal, z, and perpendicular, $\vec{b}$, components, with the z axis along $\vec{q}$. Here χ_f is the spin wave function of the final state, and $S(\vec{r})$ is the S-matrix describing the final state interaction between the debris and spectator nucleon,

$$S(\vec{r}) = 1 - \theta(z)\,\frac{\sigma_{eff}(z)(1-i\beta)}{4\pi b_0 2}\ \exp(-b^2/2b_0^2)\ , \qquad (17)$$

where β is the ratio of the real to imaginary parts of the scattering amplitude, and the step function $\theta(z)$ arises from the high energy approximation of the Glauber theory. The above

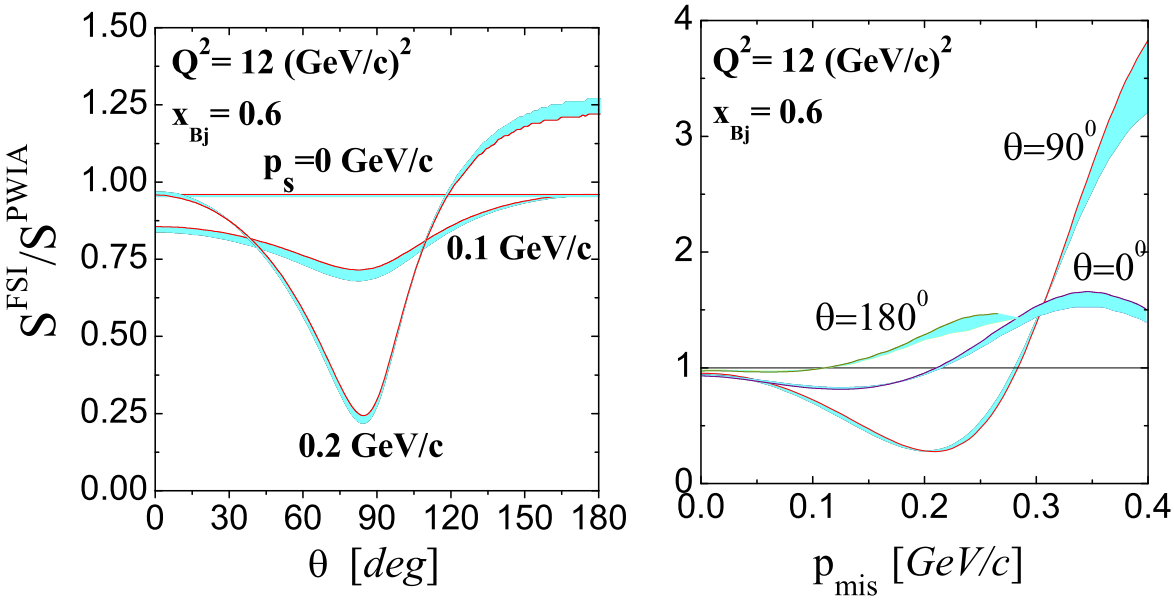

Figure 11: The momentum and angular dependence of the ratio S^{FSI}/S^{PWIA}, at $Q^2 = 12$ GeV$^2/c^2$ and $x = 0.6$ (updated calculations by the authors of [55]). Left panel: dependence on the angle between the spectator proton and the virtual photon direction. Right panel: dependence on spectator momentum.

equations can also be used to calculate quasi-elastic scattering by replacing the debris-nucleon cross section with the nucleon-nucleon cross section.

The effects of FSIs in this model are illustrated in Fig. 11, where the ratio of spectral functions with and without FSI corrections is shown as a function of θ and $|\vec{p}_s|$. For low spectator momenta, $|\vec{p}_s| \leq 100$ MeV$/c$, the effects at backward angles ($\theta \geq 130°$) are quite small, $\leq 5\%$. At larger momenta, $|\vec{p}_s| \approx 200$ MeV$/c$, FSIs introduce some 20–30% enhancement of the spectral function. The effects of FSIs become dominant at perpendicular angles, $\theta \sim 90°$, where for $|\vec{p}_s| = 200$ MeV$/c$ they reduce the ratio of spectral functions by some 75%. Of course, the study of FSI and hadronization effects is interesting in its own right, and can be pursued by focusing on the kinematical region around $\theta \sim 90°$. On the other hand, the results of the model calculations in Figs. 9 and 11 give us confidence that the effects of FSIs at backward angles are at the $\leq 5\%$ level for $|\vec{p}_s| \leq 100$ MeV$/c$, and will constitute a small correction to the impulse approximation in Eq. (8).

The combined effects of FSIs and nucleon off-shell deformation on the extracted free neutron structure function are illustrated in Fig. 12, where we plot the effective F_2^n at $x = 0.3$ and $Q^2 = 2$ (GeV$/c)^2$ normalized to the free value as a function of the kinetic energy of the spectator proton, E_{kin}. The dashed and dotted lines represent the color screening [9] and color delocalization [56] models, respectively, and curves with the squares contain FSI effects. The measured tagged neutron structure function is extrapolated to the region

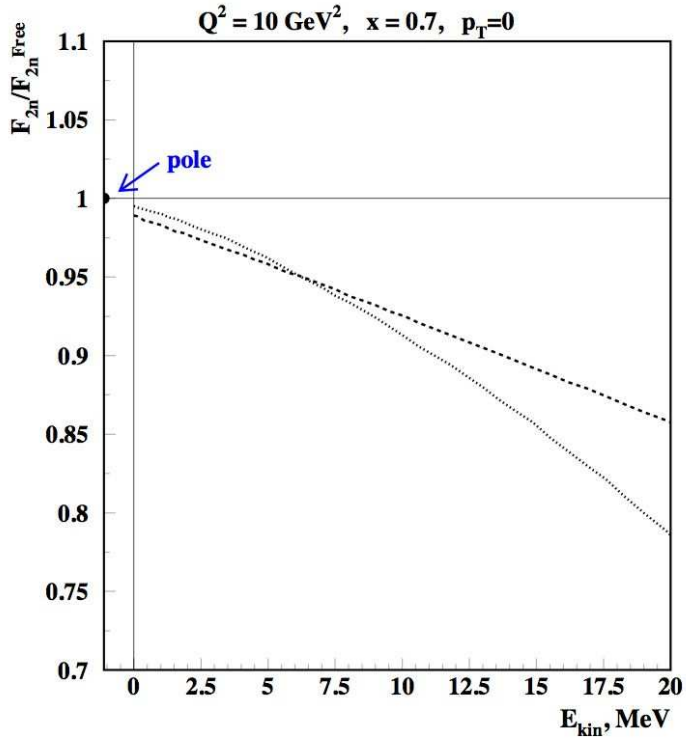

Figure 12: Effect of FSIs on the E_{kin} dependence of the extrapolated neutron structure function, normalized to the on-shell structure function, at extreme backward angles. The dashed and dotted lines represent the color screening [9] and color delocalization [56] models, respectively.

of negative values of E_{kin}, in analogy with the Chew–Low procedure for extracting the pion cross section from $p(e, e'\pi)X$ data [57], with the pole of the off-shell neutron propagator in the PWIA amplitude located at $E_{kin}^{pole} = -(|\epsilon_D| - (M_n - M_p))/2$. The virtue of such an extrapolation is that the scattering amplitudes containing final state interactions do not have singularities corresponding to on-shell neutron states. Thus, isolating the singularities through the extrapolation of effective structure functions into the negative spectator kinetic energy range will suppress the FSI effects in the extraction of the free F_2^n [48]. For the proposed kinematics, the range of spectator proton momenta would correspond to E_{kin} between 2.5 and 5 MeV. Figure 12 demonstrates that such an extrapolation can be done with the introduction of less than $\sim 2\%$ systematic error.

5 Experimental Setup and Recoil Detector

The target and recoil detector were built for the BONUS experiment E03-012 which successfully took data in Hall B in the Fall of 2005 with electron beam energies of 2.1, 4.2, and 5.3 GeV. That experiment covered the kinematical range of the nucleon resonances up to the region of deep-inelastic scattering (DIS). A new detector and target had to be built, which allowed to detect the recoiling low momentum spectator protons at backward angles.

Because of the low momenta of the protons, their energy loss is very large and the material in the path of the protons needed to be minimized to avoid too large momentum loss or absorption. Together with the requirement for the angular coverage the detector needed to be close to the target and the target itself of low density to allow the scattered protons to emerge from it. Additionally, an annulus of about 2 cm radius around the beam line needed to be kept as free as possible of materials to avoid interaction of the beam halo and Møller electrons with the target–detector assembly. The assembly had to be installed inside a solenoidal magnetic field to force the Møller electrons into trajectories spiraling in the forward direction and to provide the spectrometer magnetic field for the measurement of the curvature of the scattered protons.

The built apparatus consists of a radial time projection chamber (RTPC), 20 cm long and 14 cm in diameter, surrounding a 23 cm long target tube in its center. The target–detector system was installed inside the 5 Tesla solenoid magnet built for the DVCS experiment (E01-113). For the proposed experiment we are planning to replace the silicon vertex detector inside the central CLAS12 region by this target–detector system. This is shown in Figure 13. An overview of the capabilites of the new CLAS12 detector can be found in [58], a document prepared for PAC30.

5.1 Deuterium Target

The gas target consists of a Kapton tube, 6.1 mm in diameter and with 50 μm wall thickness, with entrance and exit windows located outside the length of the RTPC. The windows are made of 15 μm thick aluminum foil. The upstream entrance window is surrounded by an aluminum shroud to shield the RTPC from background particles created at this window. The shroud extends 47 mm into the inside of the RTPC and does not affect the acceptance for the low momentum recoil protons with very large back scattering angles. The target cell can be filled up to a pressure of 95 psia with gas. Deuterium is the primary target gas, but also hydrogen and helium will be used for calibration purposes.

5.2 Central Detector Solenoid

Both the target and the spectator proton detector will be located inside the central detector solenoidal magnet. The longitudinal magnetic field from this solenoid will force the Møller electrons into trajectories spiraling into the forward direction and, hence, suppress this background inside the recoil detector. the solenoid will also provide the analyzing magnetic field for bending the recoil proton tracks inside the RTPC for the momentum measurement.

5.3 Radial Time Projection Chamber

The cylindrical RTPC built for experiment E03-012 had to fulfill several criteria, of which the constraint to fit inside the 220 mm bore of the DVCS solenoid is not required here. The sensitive drift region of the RTPC is an annulus with the inner radius of 30 mm and an outer radius of 60 mm. Materials between the target and the sensitive detector volume had to be minimized to prevent energy loss of the scattered protons and and to minimize the

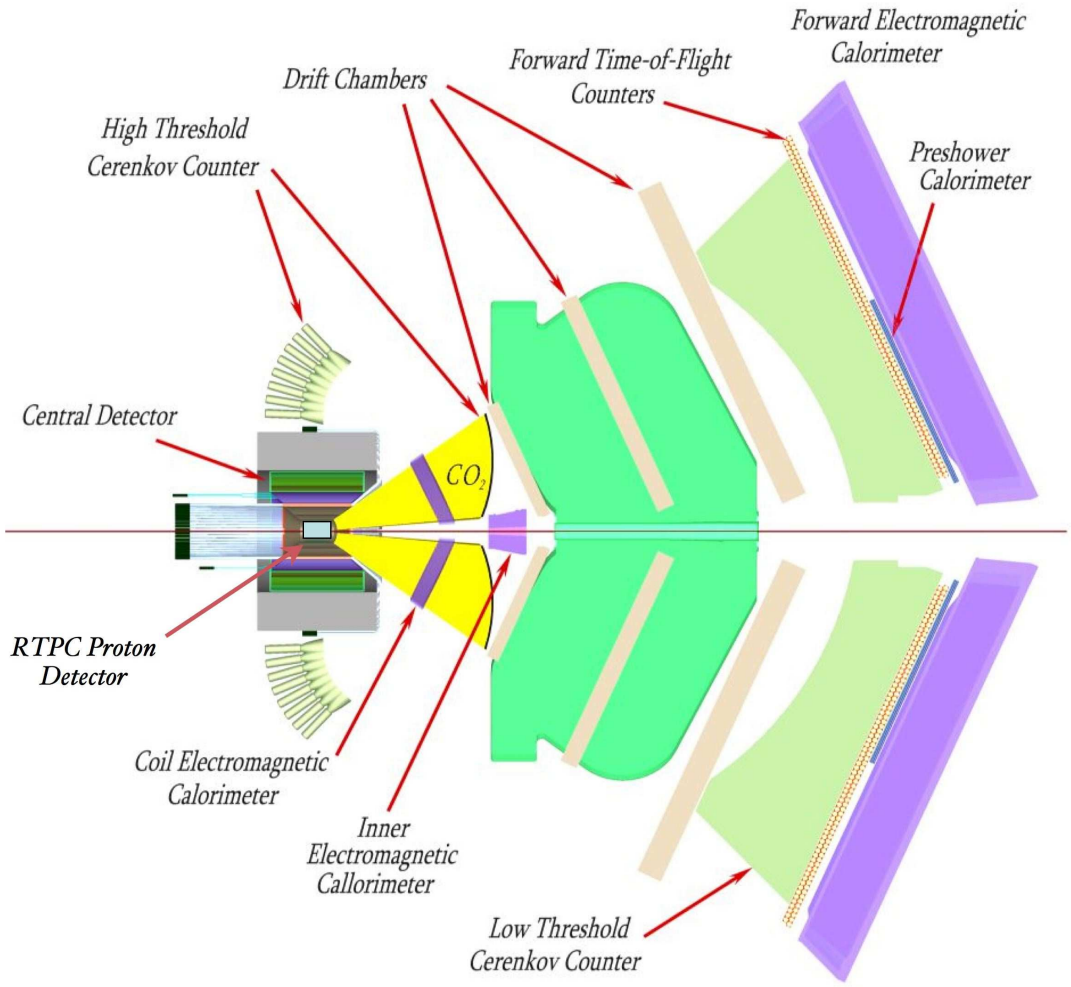

Figure 13: Thin deuterium target and radial TPC for proton detection shown inside the central detector of CLAS12.

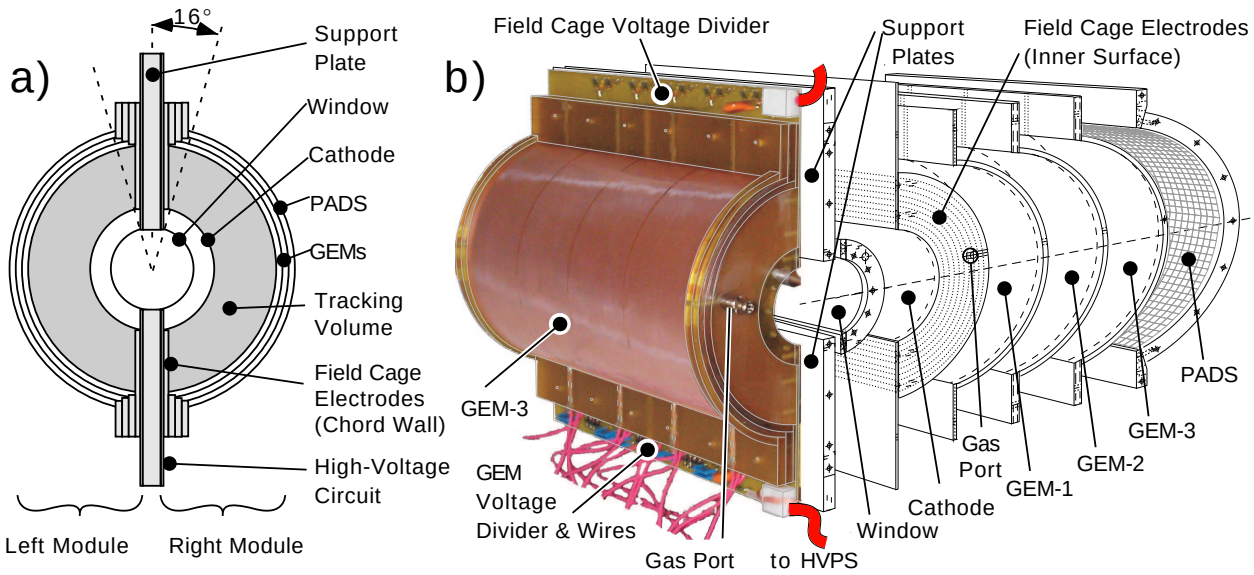

Figure 14: Photograph and Schematic Diagram of the BONUS RTPC (from [60]). a) Cross-section view through the center of the detector. b) Photograph of the left module with the readout padboard removed and a complementary exploded view exposing the components of the right module.

interaction of background particles. background particles are mostly Møller electrons forced onto helical trajectories into the forward direction along the beam axis.

The amplification of the drifting electrons is achieved by three layers of Gas Electron Multiplier (GEM, see Ref. [59]) foils at radii of 60, 63, and 66 mm. This is surrounded by a cylindrical readout surface featuring rectangular pads at a radius of 69 mm.

The resulting detector consists of two similar half-cylinder units which are mated together on either side of the central beam axis. Axial mechanical structures fit within a $\pm 16°$ wedge along the top and bottom of the assembly, as shown in Fig. 14. All of the structural components were machined out of Ultem®. Each subassembly (window, cathode, three GEMs, and padboard) is self-supporting. These parts nest together to form the whole detector module. The interior walls of the drift region (two endcaps and two vertical surfaces forming segments of a chord through the cylinder) are printed-circuit (PC) boards patterned with metal traces forming the field cage. The axial PC boards extend above and below the active portion of the detector and provide the high-voltage divider circuits and connection points, as well as pulse-injection circuitry for testing the electronics.

5.4 Custom Gas Electron Multipliers

Gas electron multipliers are 50 μm thick polyimide foils coated on both sides with 5 μm copper layer and punctured with 70 μm holes. The distance between these holes is about 140 μm. By applying a voltage in the range of 200 V to 300 V across the two copper layers a very high electric field is formed inside the holes. Electrons drifting towards the GEM foil produce an avalanche of secondary electrons when captured and accelerated through the

holes. The gain is of the order of 100. The electrons are transferred to the next GEM foil and after passing three GEM foils the resulting electron pulse is detected on the readout plane. The three GEM support frames were dimensioned such that identical GEM foils of an active area of 20 cm × 17 cm could be used throughout.

5.5 Readout Electronics

The outermost cylindrical layer of the detector is the readout board made out of a flexible polyimide substrate. It carries gold-plated conductive pads on the inner surface with a pattern of 4.45 mm × 5 mm, shown in Fig. 15. The pads are connected by closed vias to the outer surface on which groups of 16 pads are traced to a common connector, carrying 16-channel preamplifier cards.

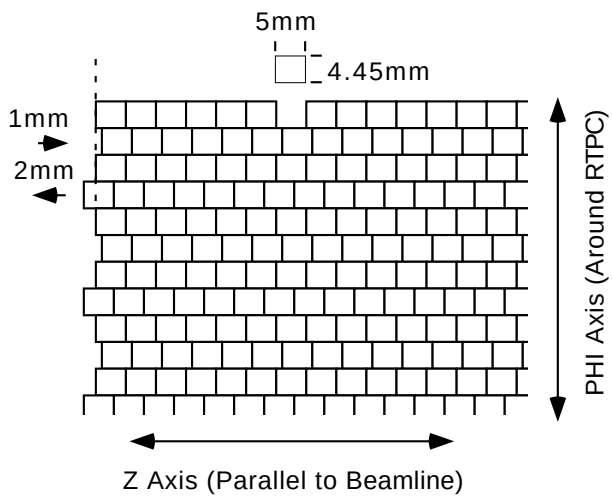

Figure 15: Pad Geometry in the Production RTPC. There are 40 rows and 40 columns of pads. Pad rows (along cylindrical axis) are offset from one-another to improve the track resolution.

The signals are inverted on these cards and transmitted via 6 m long cables to a low-impedance receiver circuit, feeding the positive signals into the readout electronics developed at CERN for the TPC of the ALICE experiment, under construction at the Large Hadron Collider for heavy-ion collisions [61]. Each readout card provides 128 channels of pre-amplification, digitization via a 10-bit ADC, signal correction circuits, and a pipeline buffer for eight events. Each event contains the signals of all pads integrated over 114 nsec time intervals for a period of 1.7 μsec before and 9.7 μsec after the arrival of an electron trigger from CLAS. Signals below preset thresholds, taking dynamically calculated and preset pedestals into account, are suppressed in the data stream to decrease the data volume for an increase of the event rate. Thirteen readout cards are needed to read out one half-cylinder of the detector. They are grouped into one crate, controlled by one readout control card (RCU). During data taking of experiment E03-012 the eight event buffer of the readout cards could not be accessed by the readout control cards, leading to an unbuffered single event readout with a limited event rate of 500 Hz. This limit will be overcome by implementing new RCU firmware from CERN in the summer of 2006.

5.6 Some First Results from 2005 Run

The RTPC was calibrated by filling the target gas cell with hydrogen gas and detecting elastic scattering events with 1.1 GeV electrons. For this data taking the GEM amplification voltage was increased to make the RTPC sensitive to minimum ionizing particles. The electrons were then detected by the RTPC and CLAS, while the RTPC also detected the elastically scattered proton in the opposite hemisphere. The electron momentum and scattering angle determined the proton kinematics, which were compared to the directly measured proton momentum by the RTPC. An event display of such an event is shown in Fig. 16 on the left.

In Fig. 17 the difference between the scattering angles as measured by CLAS and by the RTPC are displayed. The sigma of the distribution is less than 1.5°.

During data taking on the deuterium target, the electrons were only measured by CLAS, while the recoiling protons were detected by the RTPC. In Fig. 18 on the left, the correlation between electron and proton vertices is shown for 2.1 GeV beam energy. The difference between the two is shown on the right. The peak of correlated events is rising above the background of accidental events.

6 Expected Results

In this section, we describe the details of our simulation of the proposed BONUS experiment. In particular, we show that we can achieve sufficient resolution in all relevant kinematic variables and adequate statistical and systematic precision for the kinematic bins of interest.

6.1 Monte Carlo Simulation

We developed a Monte Carlo simulation for the proposed experiment to determine expected count rates, kinematic coverage and resolution. The event generator for this simulation [62] uses a parameterization of the world's structure function data on protons and deuterons and a realistic model of the deuteron momentum wave function (based on the Paris potential and the light-cone prescription by Frankfurt and Strikman [36]) to produce electron–backwards proton coincident events distributed according to the PWIA cross section in the spectator picture. This event generator has been shown to represent quite well the JLab E6 data taken at higher spectator momenta in the backward region [62]. The generated events were randomly distributed along the central (z) axis.

The backward–scattered spectator protons having an initial momentum greater than 60 MeV/c were followed through the simulation of the target and RTPC. Both energy loss and multiple scattering in all components of the target and detector were taken into account, as was the curvature of the track in the solenoid field.

A simulation of the BONUS RTPC was set up which includes proper electric and magnetic fields to correctly account for the drift of the ionization electrons in the RTPC's active volume. The proton track parameters were processed by this package to produce simulated RTPC signals. These signals were used by the RTPC analysis package to attempt reconstruction of the proton tracks. For each successfully reconstructed proton, the resulting 4-momentum and a flag indicating that the proton was detected in the RTPC were written to an output file.

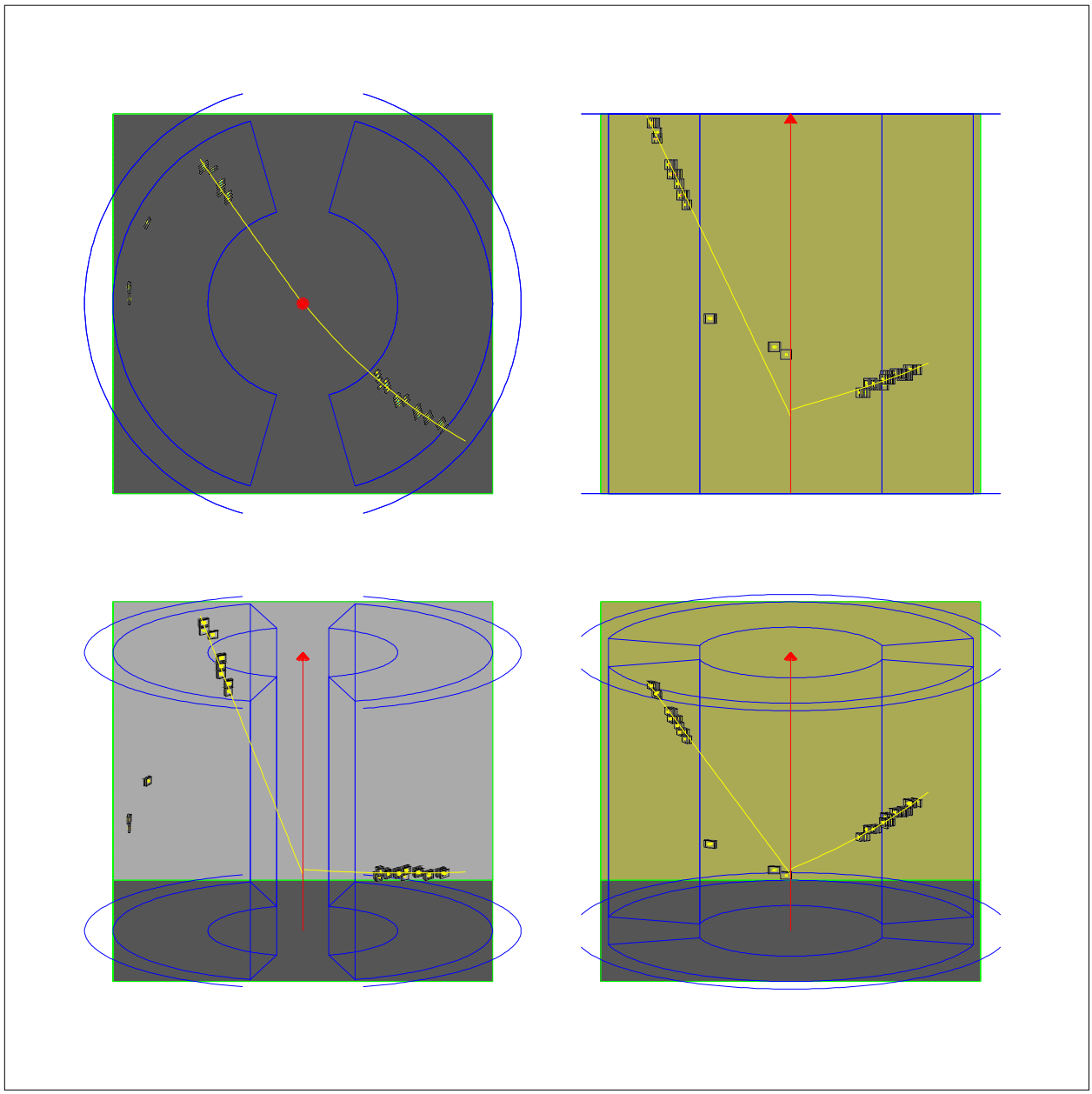

Figure 16: Elastically scattered electron (left) and proton (right) from a 1.1 GeV electron run on a hydrogen target. Top left: Cut perpendicular to the beam line (x-y-plane); top right: vertical cut (x-z-plane); bottom row: two 3D views, rotated 90° around the beam axis.

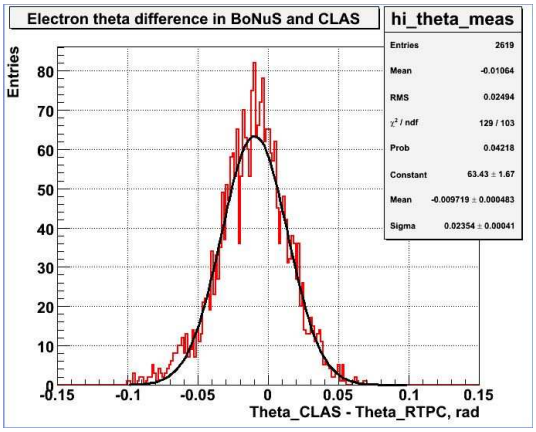

Figure 17: Difference between the electron scattering angles measured by CLAS and the RTPC using a hydrogen target and 1.1 GeV beam energy. Cuts in vertex and azimuthal scattering angle are applied.

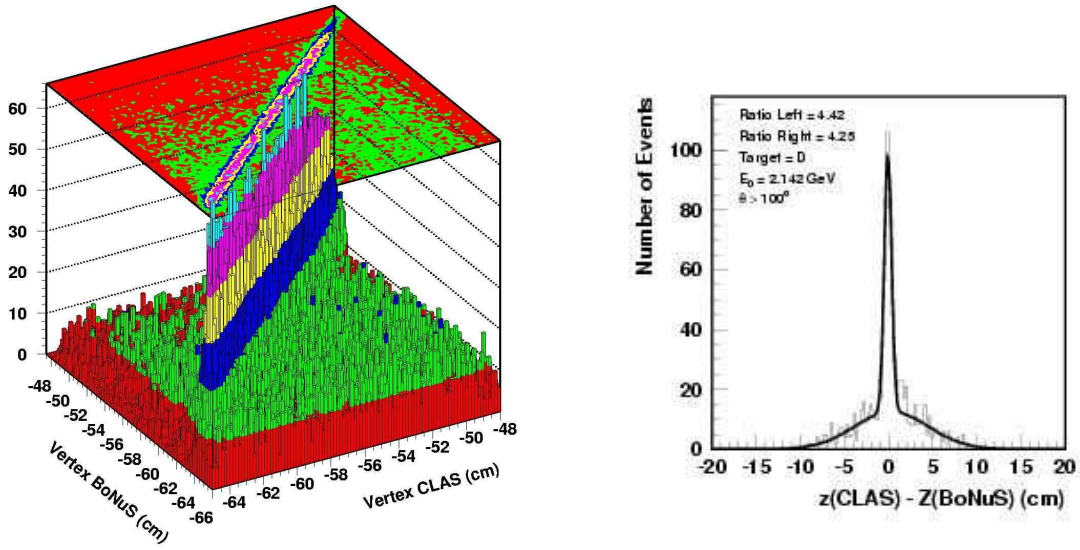

Figure 18: Vertex correlation plot between electrons as measured by CLAS and protons measured by the recoil detector (left) and difference between the two (right).

Similarly, the corresponding electron trajectories were processed by a modified version of the new CLAS12 simulation package *clasev*. The scattering-angle coverage used for the forward detector was from 5° to 40°. The new CLAS12 central detector was not included in the simulation, as it would be replaced by the RTPC for this experiment. These two simulate–analyze chains were finally combined to yield meaningful predictions of event yields, acceptance, and experimental resolutions.

For the final data sample discussed below, we considered only protons with initial momentum below 100 MeV/c and with a scattering angle of more than 90° relative to the beam and more than 110° relative to the direction of the momentum transfer vector. These very important protons (VIPs) correspond to scattering events off nearly on-shell neutrons, with very little uncertainty from final state interactions and off-shell effects (see Section 3). Fig. 19 shows the spectator momentum acceptance of the proposed experiment according to our simulation.

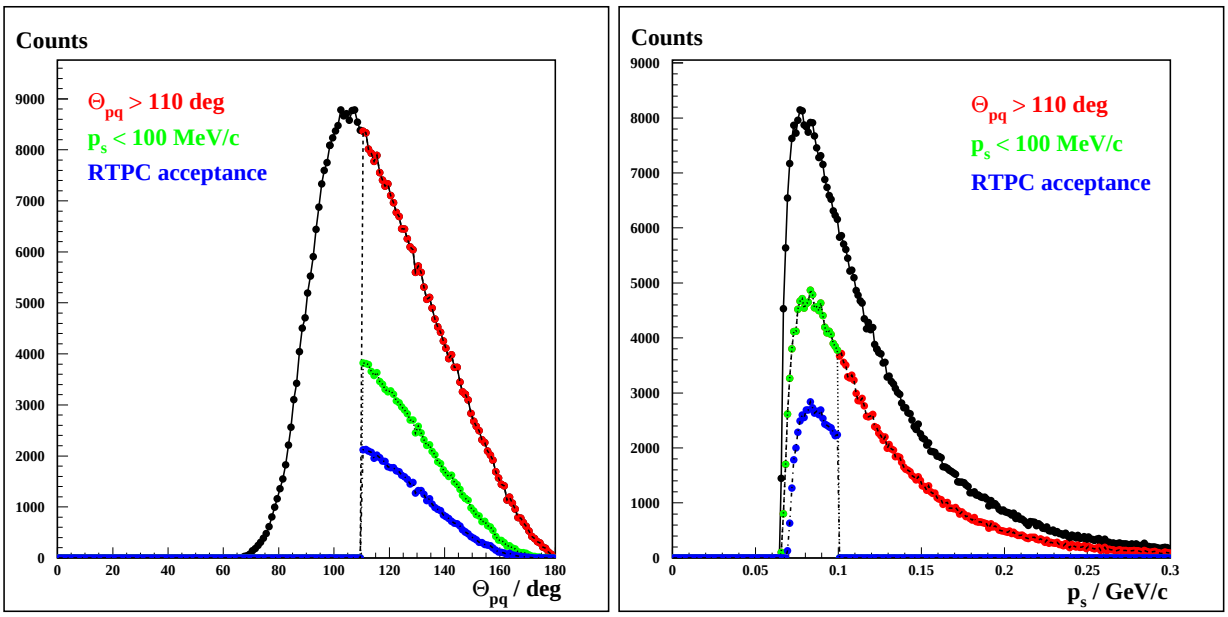

Figure 19: Influence of cuts on the expected number of counts for the proposed experiments of running at 11 GeV, plotted as a function of the angle between the spectator direction and the **q** vector, θ_{qp_s}, (left) and as a function of the spectator momentum p_s (right). Cut 1 (black points) contains all events where an electron is detected within fiducial cuts and a proton is emitted at more than 60 MeV/c momentum and at more than 90° scattering angle with respect to the beam direction. Cut 2 (red points) requires additionally that θ_{qp_s} is more than 110°. Cut 3 (green points) requires additionally that the spectator momentum is below 100 MeV/c and the final cut 4 (blue points) requires that the spectator is detected within the acceptance of the recoil detector.

It is important to note that we will be able to separate pions from protons in the RTPC detector up to momenta of at least 200 MeV/c by comparing the track curvature in the solenoid field and the energy loss in the active detector volume. We will thus be able to make a direct connection with the momentum range covered by the standard CLAS12 central tracker, which will allow us to study in detail the onset of off–shell effects and other

deviations from the simple spectator picture in a future extension of E6 to 11 GeV, and to pin down the extrapolation curve shown in Fig. 12 at the high momentum end.

6.2 Resolution

In the proposed experiment, we will use the track curvature in the solenoid field to separate protons from pions with similar energy deposit (and therefore much lower momentum) in the active detector region. On the other hand, we can use the deposited energy to calculate the initial momentum of the proton (once its identity has been established). With a 25% resolution on the deposited energy, we can achieve a resolution $\Delta p/p = 10\% \times (p/100\ \mathrm{MeV}/c)$, more than sufficient for the purpose of kinematic corrections for the initial state motion of the unobserved neutron. If we assume as a worst–case scenario that the resolution on both the track beginning and track end in the 3 cm active region is determined by the longitudinal pad size, $\sigma_z = 5\ \mathrm{mm}/\sqrt{12}$, we can still extrapolate the proton vertex to about 3 mm resolution, even including multiple scattering. This will yield a suppression of about a factor of 20 for accidental coincidences by requiring the proton and electron vertices to be within 1 cm of each other. Additionally, the timing resolution of 100 ns, corresponding to a 10 MHz rate, will reject any out of time tracks. Once a proton has been identified as being in true coincidence with a scattered electron, we can use the superior electron vertex reconstruction of CLAS12 and the average track position inside the TPC to determine the scattering angle to about 3°. The resolution in ϕ will be even better due to the narrow beam width and the smaller pad size in that direction.

Taken together, we will resolve the initial backward proton momentum to substantially better than 10 MeV/c and the relative angle between the direction of $\mathbf{q}$ and the proton to about 2°. This results in an additional uncertainty on the reconstructed missing mass W of the unobserved neutron of about 11 MeV at the elastic peak. and less at higher W, clearly much better than the expected intrinsic CLAS12 resolution.

6.3 Background Events

The largest potential source of background events comes from Møller electrons. We will set the magnetic field of the solenoid to curl up the vast majority of these electrons (up to 20 MeV). The remaining higher–momentum Møller electrons will move forward at an angle below 9° and therefore miss the RTPC recoil detector. Some of the Møller electrons with very high momenta will enter the RTPC, but will not be detected because of the insensitivity of the RTPC to minimum ionizing particles. All Møller electrons will be stopped in the downstream beam collimator. Any remaining electrons will be minimum ionizing and therefore easily distinguished from the slow protons we are interested in.

In Fig. 20 a simulation result for 5 Tesla magnetic field is shown. The silicon vertex detector in the center is partly overlayed with the outline of the RTPC as built. The drift region is highlighted in blue. As can be seen from the figure, the RTPC could be extended along the beam z-axis without interfering with the Møller electrons.

A dedicated simulation for hadronic and electromagnetic backgrounds has been set up by A. Vlassov. In the region around the beam line occupied by the RTPC the integrated rate of all backgrounds is below 200 kHz for a luminosity of $5 \cdot 10^{33}\ \mathrm{cm}^{-2}\mathrm{sec}^{-1}$. Electromagnetic

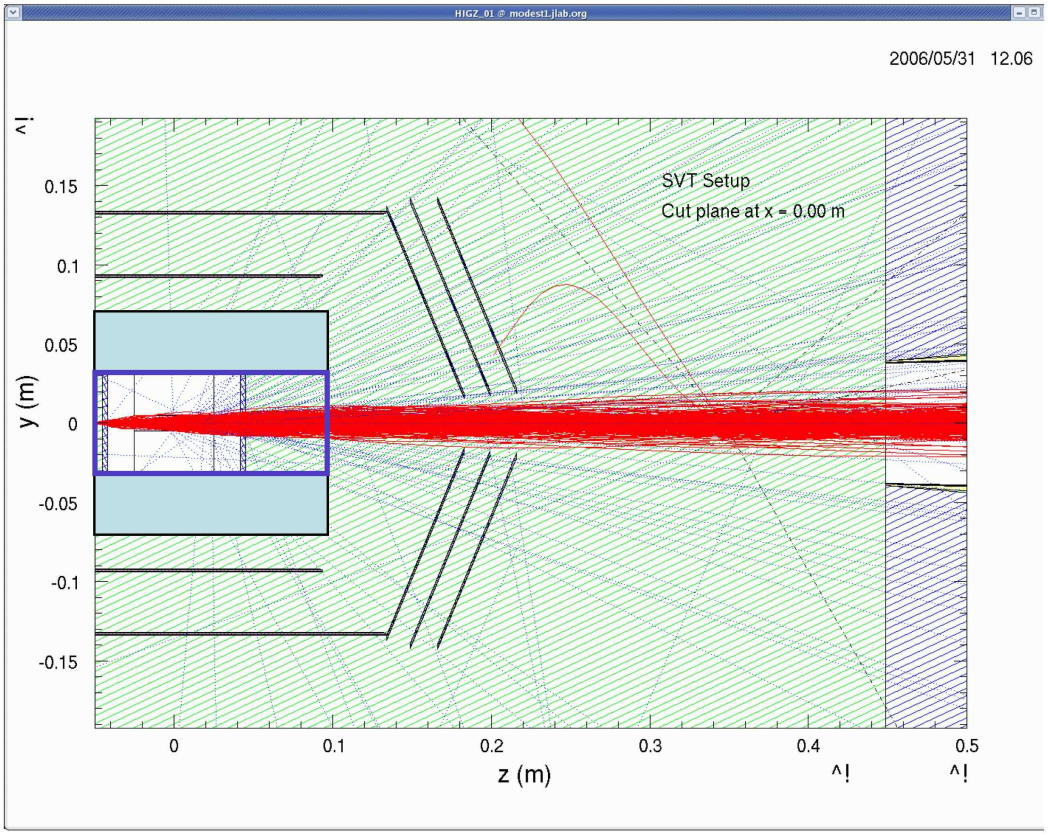

Figure 20: Simulation result of Møller electron trajectories curling around the beam solenoid (beam) axis in forward direction. The cone of trajectories clears drift region of the RTPC indicated by the blue outline overlayed on top of the silicon vertex tracker.

background accounts for about 20% of this background with photons not leaving tracks inside the RTPC's drift region, but single point-like charge deposits. The main source of the background hitting the RTPC is hadronic in the form of pions above 100 MeV/c and to a lesser extent of protons well above 100 MeV/c.

Low momentum pions are unlikely to come from high momentum transfer interactions, i.e. they are not likely to be in true coincidence with the scattered electron. Very low momentum pions will curl up in the solenoid field and not reach the recoil detector. At somewhat higher momenta (above 20 MeV/c), they can deposit a relatively large signal in the drift region of the TPC; however, they will be bent by a large angle in ϕ which can be easily detected using the azimuthal track length in the TPC. At momenta above 30 MeV/c, their energy loss in the active volume will be much smaller (by at least a factor of 3) than that of any of the protons of interest (VIPs).

The background contribution from entrance and exit window of the target can be suppressed by vertex cuts or subtracted using empty target runs. We will also use runs with hydrogen instead of deuterium as target gas to study additional background sources (as well as for calibration purposes).

About 20% of the hadronic accidental coincidence rate of about 160 kHz between scattered electrons and unrelated hadrons (pions and protons) will be below 100 MeV/c and within the acceptance of our recoil detector. We will be able to discriminate against hadrons which are more than $\pm$100 nsec out of time with the electron by extrapolating the arrival time of the drift electrons back to the entrance of the drift region. Even assuming the whole 160 kHz background and taking the time resolution results in an overall probability of 1.6% for an accidental hadron to be in time with a detected electron. The accidental rate will be further suppressed by eliminating pions (see above) and by applying a cut of $\pm$1 cm on the difference between proton and electron vertex, yielding a further reduction of background events by a factor of 20. This background can be measured by studying out–of–time and vertex–displaced coincidences and by varying the beam current (since the accidental rate varies like the luminosity squared). We can thus subtract the contribution of accidental coincidences from our signal with only slightly increasing the statistical error.

6.4 Systematic Errors

We need to know the total luminosity to extract cross sections from our data. In addition, uncertainties in the overall acceptance and trigger and cut efficiencies enter the cross section error. Experiments with the existing CLAS detector showed that an overall point-to-point error of about 5% on extracted cross sections can be achieved. We will use quasi–elastic $d(e, e'p)n$ events (scattering off the proton) to check and calibrate the simulated acceptance.

A second systematic error comes from the acceptance and efficiency of our proton recoil detector. We are using Monte-Carlo simulations of the RTPC and calibration runs to be able to calculate the uncertainty to less than 5%. For calibrations we are using events which are fully constrained kinematically, like elastic scattering on hydrogen at low beam energy or $d(e, e'p_s\pi^-p))$. In addition, the extracted cross section on the neutron depends on the integrated probability of the deuteron wave function in momentum space over the acceptance of our detector. The variation from different microscopic models of the deuteron for that probability to find a proton above our threshold of about 70 MeV/c is less than 1%.

The combined uncertainty from the sources discussed so far is about 8%. However, we can reduce this uncertainty substantially by normalizing our results for the neutron structure function F_2^n at low x (high W) to existing data from inclusive electron scattering on deuterium. In this kinematic region, the correction for nuclear effects is small. Normalizing cancels out uncertainties from sources like acceptance, detection efficiency, integral of the deuteron wave function within the acceptance, and target density, as well as FSI to some extent. We estimate a remaining error of less than 5% on the combined effects discussed above.

Additional theoretical errors come from deviations from the simple spectator picture, like breaking of factorization (less than 1%), remaining off-shell effects (up to 2% uncertainty) and final state interaction (3% to 5%) (see Section 4). We can study these effects by subdividing our data into several bins of spectator momentum and also by comparing with the results from E6, for example. Using the extrapolation method outlined towards the end of Section 4, we will be able to reduce the overall theoretical error to the order of 3%.

We estimate our overall systematic uncertainty on the extracted cross sections to be 10% at the highest values of x. Normalizing our data at low x (high W) as outlined above will reduce that systematic error to about 5% from point to point.

6.4.1 Sensitivity of F_2 Extraction on $R = \sigma_L/\sigma_T$

Extraction of the structure function F_2 from the measured cross section requires knowledge of the longitudinal to transverse cross section ratio, R. This experiment will not be capable of extracting both F_2 and R simultaneously, and will therefore have to make assumptions for the latter.

In the one photon exchange approximation, the cross section for unpolarized inclusive electron-nucleon scattering can be expressed in terms of the helicity coupling between the virtual photon and nucleon as

$$\frac{d\sigma}{d\Omega dE'} = \Gamma \left[\sigma_T(x, Q^2) + \epsilon\, \sigma_L(x, Q^2)\right], \tag{18}$$

where σ_T and σ_L are the photo-absorption cross sections for purely transverse and longitudinal virtual photons, respectively. Γ is the flux of transverse virtual photons and ϵ is the relative longitudinal flux, and are both purely kinematic factors. The F_2 structure function is directly proportional to the double differential cross section at $\epsilon = 1$, i. e. $F_2 \propto \sigma_T + \sigma_L$, and at $\epsilon < 1$ the extraction of F_2 from cross section measurements depends on both ϵ and the contribution of longitudinal strength to the total cross section.

It can be easily shown that

$$F_2 \propto \frac{d\sigma}{d\Omega dE'} \cdot \frac{1+R}{1+\epsilon\, R}, \tag{19}$$

where $R(x, Q^2) \equiv \sigma_L/\sigma_T$. To estimate the sensitivity of extracting F_2 from BONUS cross section measurements at a beam energy of 11 GeV we utilize Equation 19 and the R1990 [63] fit to both proton and deuteron measurements of R in the DIS. We note that a portion of the R1990 data set included kinematics overlapping with the proposed BONUS DIS measurements and indicates that R for the deuteron is the same as R for the proton within

the uncertainties. The percent difference of F_2 extracted from cross sections measurements utilizing R1990 and the estimated uncertainty in the fit (R1990 + dR1990) is shown in Figure 21 for electrons detected in CLAS at angles of 20, 30, and 40 degrees, and for $W < 1.8$ GeV. It is observed that the average percent difference in this kinematic range is less than 2% and significantly smaller at the largest x values and most forward angles, where $\epsilon \to 1$ and the cross section measurements are directly proportional to F_2.

While precision measurements of R in the resonance region are currently lacking for both proton and deuteron targets at higher Q^2, there now exist precision measurements from Hall C on the proton for $Q^2 < 4.5$ GeV$^2/c^2$ [64], and for the first time duality is observed in both the longitudinal and transverse structure (and hence in R). In addition to the proton resonance region data, a program [65, 66] is set to finish data taking in Hall C during early 2007 which will provide precision separations of the longitudinal and transverse cross sections for the deuteron in a kinematic region complementary to the proton measurements. Futhermore, it is expected that the continued development of global fits to the proton and deuteron longitudinal and transverse cross sections could further reduce the uncertainties on extracting F_2 from the proposed cross section measurements in the resonance region.

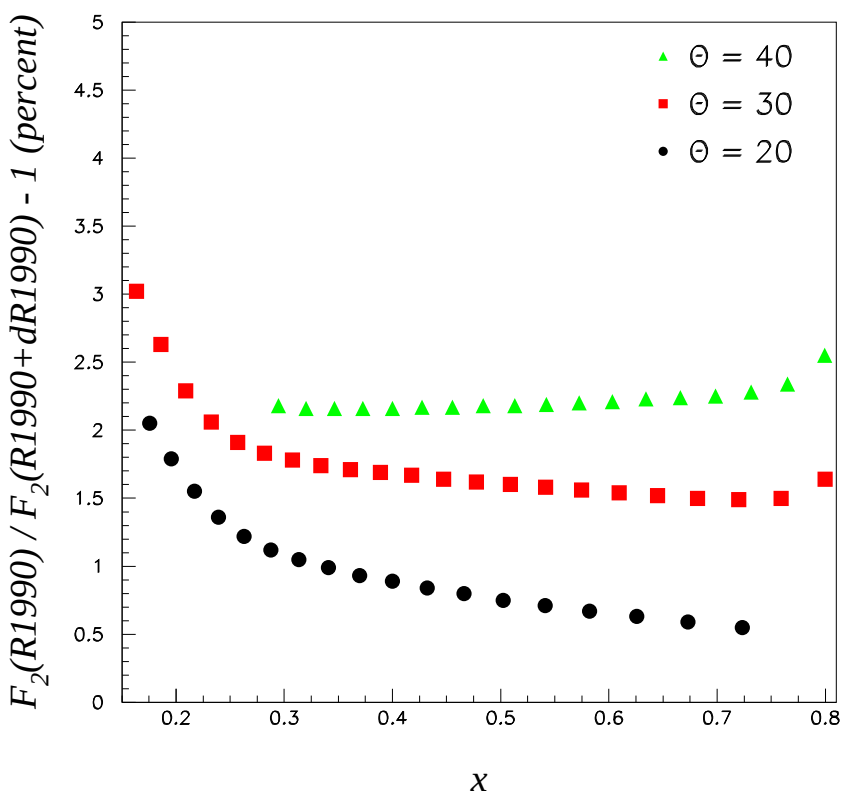

Figure 21: Percent difference between F_2 extracted from BONUS cross section measurements utilizing the R1990 parameterization and the estimated uncertainty in the fit (R1990 + dR1990).

6.5 Expected Accuracy

We propose to collect 35 days (100% efficiency) of data on deuterium with 11 GeV beam and another 5 days on hydrogen for calibration purposes. Some of the hydrogen data taking should be carried out with a low energy beam of 1 – 2.2 GeV electrons. The 30 cm long target filled with 7.5 atm deuterium gas at room temperature and the 100 nA electron beam will yield a combined luminosity of about $5 \cdot 10^{33}$ cm^{-2}s^{-1}.

Our simulation shows that under these conditions, we will collect a total of five million events with coincident detection of recoil protons below 100 MeV/c and above 110° relative to the **q** vector (VIPs) at 11 GeV. The average spectator light cone fraction will be $\alpha = 1.06$. We will cover a range in $W^\star$ from the elastic peak to about $W^\star = 4.5$ GeV and Q^2 from 1 to 14 GeV$^2/c^2$.

Inside our acceptance we expect to collect in 35 days of running a total of 38 million events, of which 31 million remain after cutting events with $W^\star > 2$ GeV. The expected results are tabulated in Table 2.

In Fig. 22, we show the kinematic range in Q^2 and x together with a cut of $W > 2$ GeV.

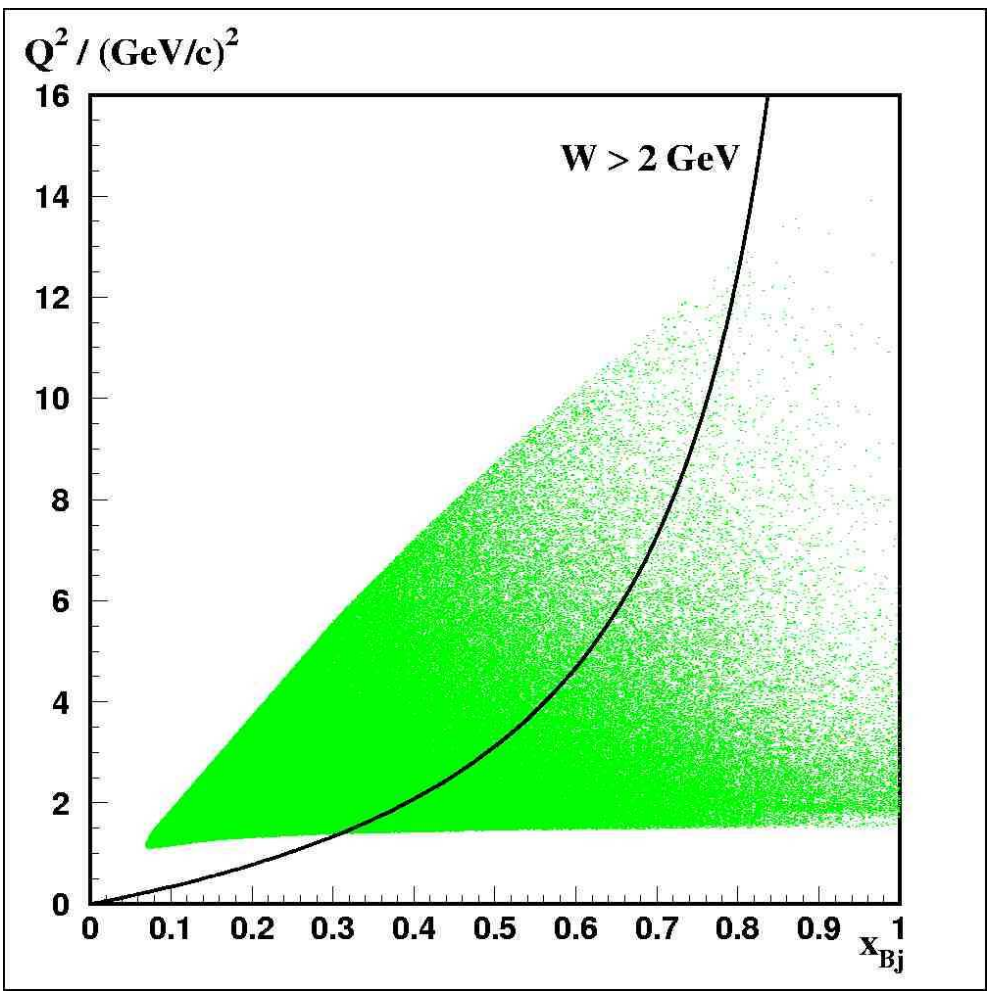

Figure 22: The kinematic range in Q^2 and x covered by this experiment, using the CLAS12 acceptance. The line correpsonds to $W = 2$ GeV.

These new 11 GeV data will allow us to expand substantially the range in $x^\star$ over which the neutron structure function F_2^n is known with good statistical precision and with small theoretical uncertainties.

Fig. 23 shows the statistical precision we can achieve for the ratio F_2^n/F_2^p as a function of $x^\star$. The curves at the bottom of the graph close to the x–axis indicate our estimate of the systematic error. The upper curve shows the total systematic error, from the combined experimental (acceptance, efficiency, event reconstruction, luminosity) and theoretical (deuteron wave function, off-shell and final state interaction effects) uncertainties. By normalizing our data to the well-known (and unambiguous) data at low x, we can extract the high–x behavior with much smaller uncertainty indicated by the lower curve.

The highest point in $x^\star$ which is still in the deep inelastic region $W^\star > 2$ GeV is at $x^\star = 0.76$, clearly in a region where valence quarks are dominant and existing data begin to become uncertain because of nuclear effects. The present upper limit in $x^\star$ is below 0.6. If we extend these data to include $W^\star > 1.8$ GeV, we can add one more point in $x^\star = 0.81$ and also significantly improve the statistical error on $x^\star = 0.76$. This is shown in Fig. 23 by the open squares data points. At these high values of Q^2 (between 6 and 12 GeV$^2/c^2$) and $W^\star$, it is likely that duality is a very good approximation and we can interpret our results directly in terms of the ratio of d/u valence quark distributions. Of course, we will be able to test duality up to $x = 0.7$ over the whole range of Q^2 and $W^\star$ using our own data.

Clearly, the high precision data set indicated in Fig. 23 will allow a comprehensive study of the x and Q^2 dependence of the structure function F_2^n in the valence region, for the first time unclouded by uncertainties from nuclear binding effects.

The same data are shown as the d/u ratio in Fig. 24, not taking the systematic errors into account.

The data we plan to collect will also allow for quark–hadron duality studies in the neutron resonance region with very good precision. Measurements in the resonance region where carried out by experiment E03-012 and are being analyzed. The expected accuracy is illustrated in Fig. 25, showing sample neutron F_2 structure function spectra at three values of Q^2, as a function of the Nachtmann scaling variable $\xi = 2x/[1 + \sqrt{1 + 4M^2x^2/Q^2}]$. Since no precise neutron resonance transition model exists yet, we actually plot the results of the existing proton resonance model, at $Q^2 = 1.0$, 1.8, and 3.0 GeV^2 (top to bottom). The dashed curve is from a parameterization of deep inelastic proton structure function data at $Q^2 = 10$ GeV^2.

Although the neutron resonance structure function and deep inelastic structure function data and parameterizations will obviously differ from the proton, we believe this is a good example of the potential quality of the neutron data attainable with BONUS. This experiment will extend the Q^2 range and add statistics to the existing BONUS measurement for $W < 2$ GeV as well as provide a more precise DIS structure function F_2^n to compare to. This is indicated by the shaded bands in the lower panel of Fig. 25 showing the statistical and systematic errors for the indicated curve at $Q^2 = 10$ GeV$^2/c^2$.

Finally, we will also be able to contribute to the world's data set on elastic neutron form factors. The expected statistical and systematic errors for each measured Q^2 at $W = M_n$ are listed in Table 1. The systematic errors will be of order 6%. The present data from E94-017 extend to $Q^2 = 5$ GeV$^2/c^2$ with a statistical error of about 0.043 in the highest

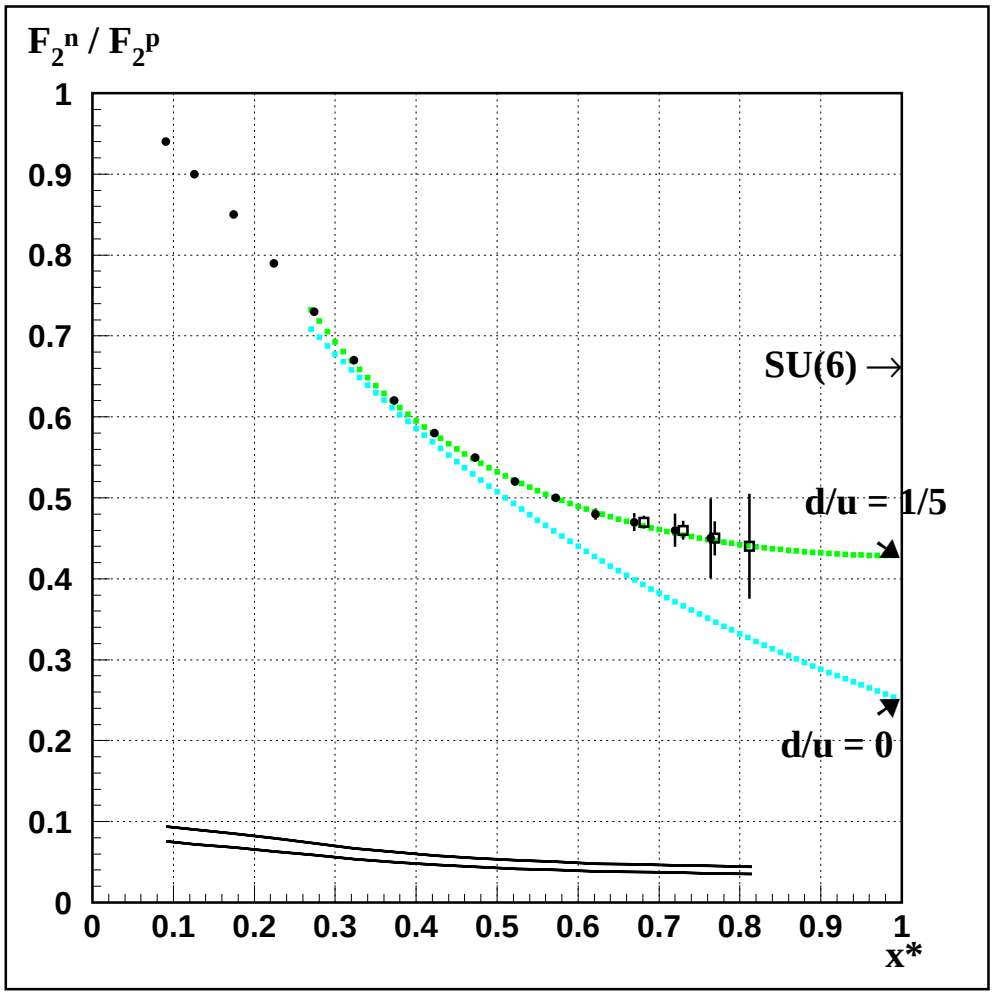

Figure 23: Ratio F_2^n/F_2^p versus $x^\star$ for spectator kinematics and $W^\star > 2$ GeV. The filled circle data points indicate the expected results of the proposed experiment with statistical error bars. The open squares data points show the improvement of the statistical error for a relaxed cut of $W^\star > 1.8$ GeV (the two lower $x^\star$ points are shifted slightly towards higher $x^\star$). The underlying coloured curves are duality based model calculations for different scenarios of SU(6) symmetry breaking from [18]. The naive SU(6) prediction for the $x^\star \to 1$ is indicated on the ordinate. The curves at the bottom of the figure indicate the estimated systematic error. The upper curve takes combines the experimental and theoretical uncertainties, while the lower curve represents the systematic error estimate due to experimental and theoretical uncertainties for the point-to-point error after normalization at low x.

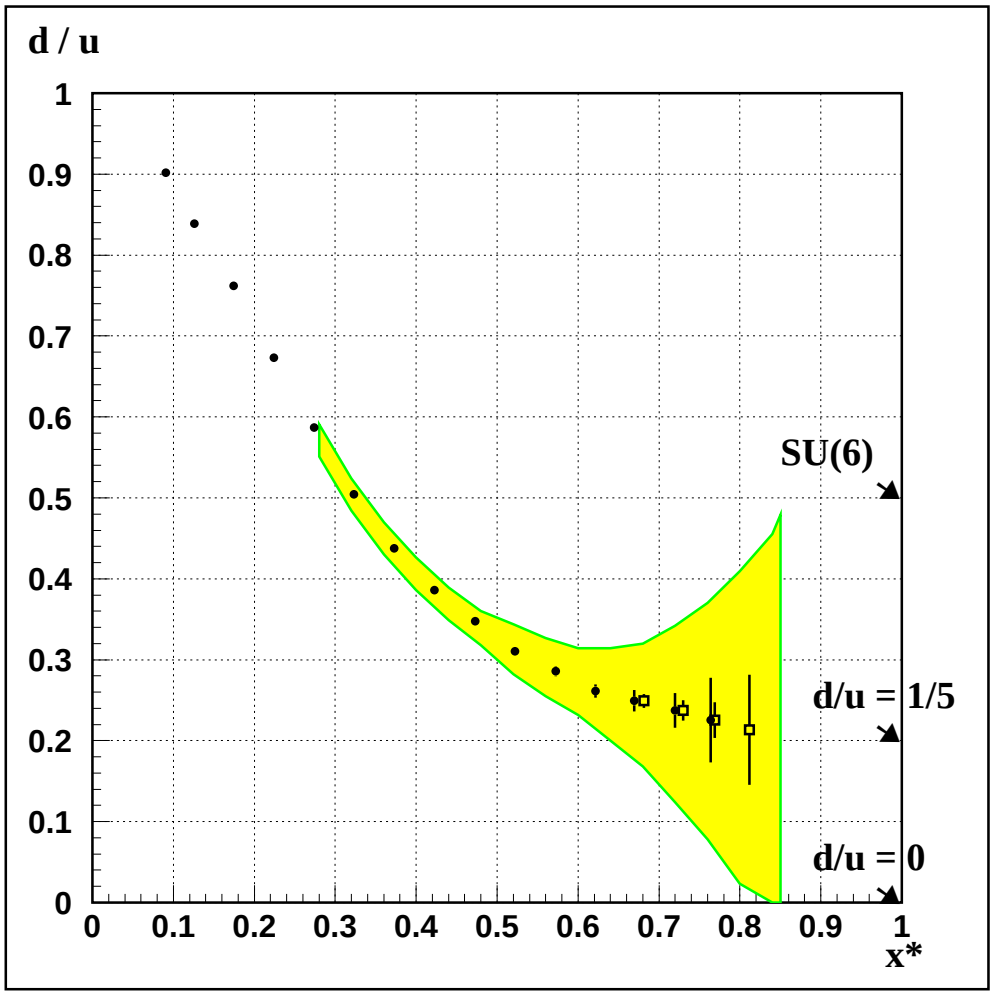

Figure 24: Ratio of d/u quarks versus $x^\star$ converted from the data points shown in Fig. 23. The shaded band indicates the present uncertainty in extracting the d/u ratio from the existing data.

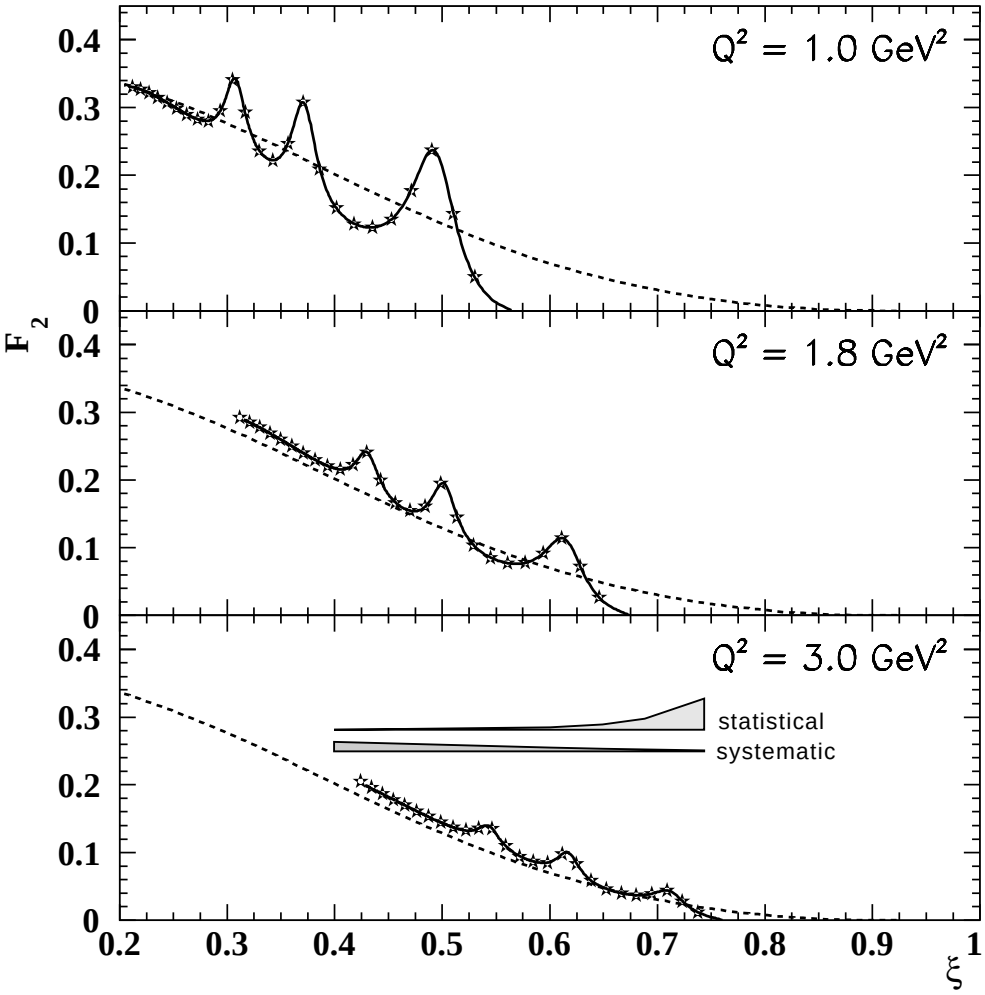

Figure 25: Sample neutron F_2 structure function spectra at Q^2 = 1.0, 1.8 and 3.0 GeV^2, plotted as a function of the Nachtmann scaling variable ξ. This graph shows the expected accuracy after analyzing the data taken by E03-012. Since the neutron structure function in the resonance region is unknown, the curves depict a parameterization of proton resonance region data (solid curve) and the NMC fit of deep inelastic structure function data at Q^2 = 10 GeV^2 (dashed curve). The statistical uncertainty is smaller than the symbols, and is typically 0.6%, 1%, and 2-3%, at Q^2 = 1.0, 1.8, and 3.0 GeV^2, respectively. The error bands on the Q^2 = 3 GeV$^2/c^2$ panel indicate the precision to which theDIS F_2^n structure function will be measured by the present proposal.

Q^2-range / $(\mathrm{GeV}/c)^2$	No. of Events	Rel. Stat. Err.
2.0 – 2.5	4215	0.015
2.5 – 3.0	3333	0.017
3.0 – 3.5	1870	0.023
3.5 – 4.0	1000	0.032
4.0 – 4.5	570	0.042
4.5 – 5.0	365	0.052
5.0 – 6.0	355	0.053
6.0 – 7.0	150	0.082
7.0 – 9.0	86	0.108

Table 1: Expected relative statistical error for the measurement of the normalized magnetic form factor of the neutron.

Q^2-bin. We can normalize our results at small Q^2, where good precision data are available, and can extract the elastic cross section with good accuracy at the higher Q^2, where we can compare our result with E94-017 up to $Q^2 = 5$ GeV$^2/c^2$ and extend the Q^2 range beyond (see Tab. 1). This will allow us to determine the absolute magnitude of the form factor G_M^n with a largely independent method.

6.6 Upgrade Possibilities for the RTPC

With a modest investment into upgrades of the existing RTPC or by replacing the RTPC with a new one, while keeping the readout electronics or adding some readout channels, the experiment proposed here could be improved. Several of these improvements could be financed by outside grants to be obtained by university groups involved with the experiment.

The necessary and above mentioned increase in readout speed by upgrading the readout controller unit (RCU) internal software (firmware) is expected to actually yield more of an improvement than the increase to 1 kHz. In the present readout scheme, the trigger provided by the CLAS detector initiates the transfer of the properly timed RTPC event 11.2 μsec long. Only after the complete transfer of that event to the CLAS DAQ and readout of all other CLAS detector components can a new trigger be issued. The new firmware will be able to use the ring buffer of eight events available on the front-end readout cards. In this mode of buffered readout operation, new triggers can be issued before an event is read out completely. This will reduce largely or eliminate completely the dead time of the RTPC readout and will increase the overall readout rate from the present 500 Hz to above 1 kHz.

The RCU presently used, a laboratory version of the ALICE TPC readout controller, is able to control 14 front-end cards and communicate and transfer data via an Universal Serial Bus (USB 2.0) to the crate controller. A further increase in readout speed may be possible by switching ALICE's main readout control system, using a central RCU with separate trigger and optical data transfer control cards. This system is not using a commercial standard and features PCI based receiver cards. Besides a modest investment of less than 10,000 USD for the purchase of these readout boards, a new implementation into the CLAS readout will be necessary, which will be upgraded for the new CLAS12 detector.

An increase in luminosity by increasing the length of the target gas cell would reduce the data taking time, while keeping the event to background ratio constant. A doubled target gas cell will approximately double the data rate. A longer target gas cell would require the design and construction of a longer RTPC. An increases range of angular backward scattering anlges of the spectator protons would be a byproduct. To not loose position (momentum) resolution, additional readout channels would need to be purchased.

To improve the momentum resolution of the spectator protons we studied the effect of increasing the radial drift region from the present 3 cm to 6 cm. The same RTPC simulation as used for the spectator proton acceptance studies was employed and yielded a relative improvement of 50%.

7 Summary and Beam Time Request

We propose to measure the structure function F_2^n of the neutron by scattering 11 GeV electrons off a deuterium gas target and detecting the scattered electron and recoiling proton. By selecting very backward scattering angles and very low recoil momenta for the proton, scattering events on almost free neutrons can be selected. This is particularly important at high x-Bjorken where Fermi motion effects in inclusive measurements are substantial.

For the detection of the recoil protons we propose to install the existing radial time projection chamber and target gas cell assembly which has been successfully used during the BONUS experiment E03-012. The RTPC can detect proton recoil momenta down to a lower limit of 70 MeV/c while being insensitive to minimum ionizing particles. We would use the upgraded CLAS12 forward spectrometer.

The deep-inelastic scattering data, $W^\star > 2GeV$, extend to $x^\star$ as high as 0.8, allowing for an extraction of the ratio F_2^n/F_2^p.

Comparing the data from the deep inelastic region extended to larger x with those from the resonance region, we can test duality for the neutron. The present proposal will increase the Q^2 range in the resonance region covered so far by experiment E03-012 and provide more statistics.

We request 35 days of 11 GeV beam using a deuterium gas target. As demonstrated in the previous section, this will allow us to collect high precision data on the neutron, with good statistics, resolution and kinematic coverage, and with minimal uncertainties due to nuclear binding effects. The beam time request was optimized to guarantee that the measurement is not statistics-limited. In addition, the statistical errors listed in the previous section assume that the whole data set for spectator momenta from 70 to 100 MeV/c will be integrated over. For most bins, the statistical precision will be good enough to allow us to study the dependence of the extracted structure functions on the spectator variables (momentum p_s, light cone fraction α and angle relative to the $\mathbf{q}$ vector).

In addition to the 35 days of data taking on deuterium we require 3 days of 11 GeV beam and 1 day of 1 - 2.2 GeV beam using a hydrogen target for commissioning and calibration purposes, and 1 more day on an empty target for background studies.

Finally, we request resources from JLab to support the installation and integration into CLAS12 of the RTPC recoil detector. We also request support of JLab staff to support the integration of the RTPC readout into the new CLAS12 data acquisition software. Using our previous experience obtained during installation of experiment E03-012 we estimate that two weeks of setup time in the Hall will be needed for installation and decomissioning of the target–detector system, including check-out without beam.

In total, we request 40 days of new beam time in Hall B for the program of neutron structure measurements described in this proposal, using the new CLAS12 detector.

References

[1] G. Dodge, *et al.*, *The Structure Function of the Free Neutron via Spectator Tagging*, JLab E03-012 Proposal to PAC23 (2003).

[2] R.P. Feynman, *Photon Hadron Interactions* (Benjamin, Reading, Massachusetts, 1972); F.E. Close, Phys. Lett. **B43**, 422 (1973); Nucl. Phys. **B80**, 269 (1973); R.D. Carlitz, Phys. Lett. **B58**, 345 (1975); N. Isgur, Phys. Rev. D **59**, 034013 (1999).

[3] A.D. Martin, R.G. Roberts, W.J. Stirling and R.S. Thorne, Eur. Phys. J. C **14**, 133 (2000); H.L. Lai, *et al.*, Eur. Phys. J. C **12**, 375 (2000); M. Glück, E. Reya and A. Vogt, Eur. Phys. J. C **5**, 461 (1998).

[4] G.R. Farrar and D.R. Jackson, Phys. Rev. Lett. **35**, 1416 (1975).

[5] S. Kuhlmann, *et al.*, Phys. Lett. B **476**, 291 (2000).

[6] L.W. Whitlow, *et al.*, Phys. Lett. B **282**, 475 (1992); A. Bodek, S. Dasu and S.E. Rock, in Tucson Part. Nucl. Phys., 768 (1991), SLAC-PUB-5598.

[7] W. Melnitchouk and A.W. Thomas, Phys. Lett. **B377**, 11 (1996).

[8] W. Melnitchouk and J.C. Peng, Phys. Lett. **B400**, 220 (1997).

[9] L.L. Frankfurt and M.I. Strikman, Nucl. Phys. **B250**, 1585 (1985); Phys. Rep. **160**, 235 (1988).

[10] I. Niculescu, *et al.*, Phys. Rev. Lett. **85**, 1186 (2000); I. Niculescu, *et al.*, Phys. Rev. Lett. **85**, 1182 (2000); R. Ent, C.E. Keppel and I. Niculescu, Phys. Rev. D **62**, 073008 (2000); S. Liuti, R. Ent, C.E. Keppel and I. Niculescu, Phys. Rev. Lett. **89**, 162001 (2002);

[11] J. Arrington, J. Crowder, R. Ent, C.E. Keppel and I. Niculescu, *Proceedings of the 9th Int. Conf. on the Structure of Baryons 2002*, 550 (2002); J. Arrington, *et al.* Phys. Rev. C **64**, 014602 (2001).

[12] A. Airapetian, *et al.* (HERMES Collaboration), Phys. Rev. Lett. **90**, 092002 (2003);

[13] N. Isgur, S. Jeschonnek, W. Melnitchouk and J.W. Van Orden, Phys. Rev. D **65**, 054005 (2001); S. Jeschonnek and J.W. Van Orden, Phys. Rev. D **65**, 094038 (2002); V.V. Davidovsky and B.V. Struminsky, hep-ph/0205130; G. Ricco, M. Anghinolfi, M. Ripani, S. Simula and M. Taiuti, Phys. Rev. C **57**, 356 (1998).

[14] F.E. Close and N. Isgur, Phys. Lett. B **509**, 81 (2001).

[15] W. Melnitchouk, R. Ent and C.E. Keppel, Phys. Report **406**, 127 (2005).

[16] A. De Rujula, H. Georgi and H.D. Politzer, Ann. Phys. **103**, 315 (1977); H. Georgi and H.D. Politzer, Phys. Rev. D **14**, 1829 (1976).

[17] E.D. Bloom and F.J. Gilman, Phys. Rev. D **4**, 2901 (1970).

[18] F.E. Close and W. Melnitchouk, Phys. Rev. C **68**, 035210 (2003).

[19] W. Brooks, *et al.*, JLab E94-017, www.jlab.org/exp_prog/proposals/94/PR94-017.pdf

[20] J.D. Lachniet, *A high precision measurement of the neutron magnetic form factor using the CLAS detector*, Dissertation, Carnegie Mellon University (2005).

[21] J.D. Sullivan, Phys. Rev. D **5**, 1732 (1972).

[22] A. Thomas, Phys. Lett. B **126**, 97 (1983).

[23] P. Amaudruz, *et al.* (NMC), Phys. Rev. Lett. **66**, 2712 (1991); P. Amaudruz, *et al.* (NMC), Phys. Rev. D **50**, R1 (1994).

[24] K. Gottfried, Phys. Rev. Lett. **18**, 1174 (1967).

[25] A. Baldit, *et al.*, Phys. Lett. B **332**, 244 (1994).

[26] E.A. Hawker, *et al.* (E866 Collaboration), Phys. Rev. Lett. **80**, 3715 (1998).

[27] J.C. Peng, *et al.* (E866 Collaboration), Phys. Rev. D **58**, 092004 (1998).

[28] R.S. Towell, *et al.* (E866 Collaboration), Phys. Rev. D **64**, 052002 (2001).

[29] K. Akerstaff, *et al.* (HERMES Collaboration), Phys. Lett. B **464**, 123 (1999).

[30] S. Kumano, Phys. Rep. **303**, 183 (1998).

[31] J.P. Speth and A.W. Thomas, Adv. Nucl. Phys. **24**, 83 (1998).

[32] G.T. Garvey and J.C. Peng, Prog. Part. Nucl. Phys. **47**, 203 (2001).

[33] C. Adloff, *et al.* (H1 Collaboration), Eur. Phys. J. **C6**, 587 (1999).

[34] P.M. King, *et al.*, Jefferson Lab Letter of Intent LOI-05-001, (2004).

[35] I.R. Afnan, *et al.*, Phys. Lett. B **493**, 36 (2000).

[36] L.L. Frankfurt and M.I. Strikman, Phys. Rep. **76**, 217 (1981).

[37] C. Ciofi degli Atti and S. Simula, Phys. Lett. **B319**, 23 (1993); Few-Body Systems **18**, 55 (1995); S. Simula, Phys. Lett. **B387**, 245 (1996); Few-Body Systems Suppl. **9**, 466 (1995).

[38] W. Melnitchouk, M. Sargsian and M.I. Strikman, Z. Phys. **A359**, 99 (1997).

[39] See e.g. R.P. Bickerstaff and A.W. Thomas, J. Phys. G **15**, 1523 (1989).

[40] W. Melnitchouk, A.W. Schreiber and A.W. Thomas, Phys. Lett. **B335**, 11 (1994); Phys. Rev. D **49**, 1183 (1994).

[41] G.D. Bosveld, A.E.L. Dieperink and A.G. Tenner, Phys. Rev. C **49**, 2379 (1994).

[42] F. Gross and S. Liuti, Phys. Rev. C **45**, 1374 (1992); S. Liuti and F. Gross, Phys. Lett. **B356**, 157 (1995).

[43] S.A. Kulagin, G. Piller and W. Weise, Phys. Rev. C **50**, 1154 (1994); S.A. Kulagin, W. Melnitchouk, G. Piller and W. Weise, Phys. Rev. C **52**, 932 (1995).

[44] S.I. Alekhin, S.A. Kulagin and S. Liuti, Phys. Rev. D **69**, 114009 (2004).

[45] L. Heller and A.W. Thomas, Phys. Rev. C **41**, 2756 (1990).

[46] S. Dieterich, *et al.*, Phys. Lett. **B500**, 47 (2001); R. Ransome, Nucl. Phys. **A699**, 360 (2002).

[47] W. Melnitchouk, K. Tsushima and A.W. Thomas, Eur. Phys. J. A **14**, 105 (2002).

[48] M. Sargsian and M. Strikman, hep-ph/0511054.

[49] L.L. Frankfurt, *et al.*, Z. Phys. **A352**, 97 (1995); Phys. Lett. **B369**, 201 (1996).

[50] C. Ciofi degli Atti and B.Z. Kopeliovich, Eur. Phys. J. A **17**, 133 (2003).

[51] M.I. Strikman, M. Tverskoy and M. Zhalov, nucl-th/9609055, *Proceedings of Workshop "Future Physics at HERA"*, Hamburg, 1085 (1996).

[52] M.R. Adams, *et al.*, Phys. Rev. Lett. **74**, 5198 (1995).

[53] B.Z. Kopeliovich, J. Nemchik and E. Predazzi, hep-ph/9511214, *Proceedings of the ELFE Summer School on Confinement Physics*, ed. S.D. Bass and P.A.M. Guichon, Editions Frontieres, Gif-sur-Yvette, 391 (1995).

[54] C. Ciofi degli Atti, L.P. Kaptari and D. Treleani, Phys. Rev. C **63**, 044601 (2001).

[55] C. Ciofi degli Atti, L.P. Kaptari and B.Z. Kopeliovich, Eur. Phys. J. A **19**, 145 (2004).

[56] F.E. Close, R.G. Roberts and G.G. Ross, Phys. Lett **B129**, 346 (1983).

[57] G.F. Chew and F.E. Low, Phys. Rev. **113**, 1640 (1959).

[58] E. Elouadrhiri, *An Overview of the CLAS12 Spectrometer*, CLAS12 Document to PAC30 (2006).

[59] F. Sauli, Nucl. Instrum. and Meth. **A386**, 531 (1997).

[60] H. Fenker, *et al.*, to appear in Nucl. Instrum. and Meth. (2006).

[61] L. Musa, *et al.*, Proc. of IEEE Nuclear Science Symposium 2003, Portland, USA (2003).

[62] A.V. Klimenko, S.E. Kuhn, *et al.*, Phys. Rev. C **73**, 035212 (2006).

[63] L.W. Whitlow, *et al.*, Phys. Lett. B **250**, 193 (1990).

[64] Y. Liang, M.E. Christy, *et al.*, nucl-ex/0410027.

[65] M.E. Christy, *et al.*, JLab E02-109, www.jlab.org/exp_prog/proposals/02/PR02-109.ps

[66] J. Arrington, *et al.*, JLab E06-009, www.jlab.org/exp_prog/proposals/06/PR06-009.pdf

$Q^2/(\mathrm{GeV}^2/c^2)$	x	W/GeV	E'/GeV	No. of Events	Rel. Stat. Err.
1.2	0.085	3.748	3.324	857922	0.001
1.3	0.118	3.205	5.050	665818	0.001
1.3	0.165	2.709	6.316	83760	0.003
1.3	0.218	2.275	6.025	4438	0.015
1.3	0.270	1.989	6.342	455	0.047
1.2	0.320	1.741	5.595	170	0.077
1.4	0.089	3.914	2.640	762382	0.001
1.4	0.123	3.334	4.629	1815651	0.001
1.4	0.173	2.786	6.406	1155466	0.001
1.5	0.223	2.435	7.373	664282	0.001
1.5	0.273	2.182	7.992	379996	0.002
1.5	0.323	1.986	8.436	234723	0.002
1.5	0.373	1.827	8.777	157108	0.003
1.5	0.423	1.698	9.029	103278	0.003
1.5	0.474	1.580	9.221	64129	0.004
1.5	0.523	1.487	9.369	41595	0.005
1.5	0.573	1.396	9.484	27256	0.006
1.5	0.623	1.321	9.628	19460	0.007
1.5	0.673	1.248	9.729	16729	0.008
1.5	0.724	1.181	9.755	11608	0.009
1.5	0.764	1.122	9.851	3129	0.018
1.5	0.815	1.014	9.610	625	0.040
1.5	0.876	0.937	9.775	569	0.042
1.7	0.094	4.120	1.857	263118	0.002
1.7	0.125	3.589	3.590	1753627	0.001
1.7	0.174	3.001	5.606	1404756	0.001
1.7	0.224	2.604	6.815	1016282	0.001
1.7	0.274	2.319	7.574	756179	0.001
1.7	0.324	2.098	8.106	557418	0.001
1.7	0.374	1.921	8.498	445548	0.001
1.7	0.424	1.776	8.790	353479	0.002
1.7	0.474	1.653	9.024	257370	0.002
1.7	0.525	1.544	9.220	197224	0.002
1.7	0.573	1.451	9.369	146922	0.003
1.7	0.624	1.366	9.493	99238	0.003
1.7	0.675	1.283	9.618	92068	0.003

Table 2: Expected relative statistical error on each data point within the kinematic coverage with 11 GeV beam energy (continued on next page).

$Q^2/(\mathrm{GeV}^2/c^2)$	x	W/GeV	E'/GeV	No. of Events	Rel. Stat. Err.
1.7	0.723	1.220	9.706	90475	0.003
1.7	0.770	1.160	9.776	44099	0.005
1.8	0.816	1.073	9.692	7909	0.011
1.7	0.875	0.939	9.704	3072	0.018
1.7	0.926	0.938	9.768	6145	0.013
1.8	0.976	0.938	9.868	14737	0.008
1.9	0.097	4.322	1.404	13884	0.008
2.0	0.129	3.813	2.638	1108806	0.001
2.0	0.174	3.249	4.616	1268759	0.001
2.0	0.224	2.815	6.020	974231	0.001
2.0	0.274	2.499	6.931	734670	0.001
2.0	0.324	2.257	7.558	551785	0.001
2.0	0.374	2.060	8.012	428363	0.002
2.0	0.424	1.898	8.371	356779	0.002
2.0	0.474	1.757	8.658	274214	0.002
2.0	0.524	1.638	8.873	216344	0.002
2.0	0.574	1.531	9.064	164904	0.002
2.0	0.623	1.437	9.207	115569	0.003
2.0	0.674	1.346	9.355	82508	0.003
2.0	0.725	1.266	9.472	79948	0.004
2.0	0.773	1.196	9.556	64812	0.004
2.1	0.817	1.125	9.579	18208	0.007
2.1	0.874	0.951	9.285	2276	0.021
2.0	0.932	0.939	9.566	5519	0.013
2.0	0.984	0.938	9.785	63389	0.004
2.4	0.138	3.983	1.932	439800	0.002
2.4	0.175	3.520	3.456	1062657	0.001
2.4	0.224	3.048	5.081	890413	0.001
2.4	0.274	2.698	6.160	675207	0.001
2.4	0.324	2.432	6.901	506946	0.001
2.4	0.374	2.216	7.447	386938	0.002
2.4	0.424	2.031	7.867	313135	0.002
2.4	0.474	1.877	8.193	260272	0.002
2.4	0.524	1.744	8.473	199500	0.002
2.4	0.574	1.623	8.678	144362	0.003
2.4	0.623	1.515	8.883	116252	0.003

Table 2 (continued): Expected relative statistical error on each data point within the kinematic coverage with 11 GeV beam energy (continued on next page).

$Q^2/(\mathrm{GeV}^2/c^2)$	x	W/GeV	E'/GeV	No. of Events	Rel. Stat. Err.
2.4	0.674	1.418	9.030	84159	0.003
2.4	0.725	1.322	9.164	64129	0.004
2.4	0.775	1.241	9.303	59577	0.004
2.4	0.820	1.170	9.358	30727	0.006
2.5	0.867	1.050	9.172	3641	0.017
2.4	0.933	0.939	9.279	2731	0.019
2.4	0.985	0.938	9.541	41652	0.005
2.8	0.144	4.155	1.486	52236	0.004
2.9	0.177	3.772	2.373	701610	0.001
2.9	0.224	3.299	3.995	728354	0.001
2.9	0.274	2.920	5.237	592186	0.001
2.9	0.324	2.625	6.134	458863	0.001
2.9	0.374	2.383	6.786	339367	0.002
2.9	0.424	2.185	7.274	263118	0.002
2.9	0.474	2.010	7.672	211393	0.002
2.9	0.524	1.860	7.983	175943	0.002
2.9	0.574	1.727	8.257	133266	0.003
2.9	0.624	1.606	8.470	96393	0.003
2.9	0.674	1.495	8.655	75054	0.004
2.9	0.724	1.392	8.799	52236	0.004
2.9	0.775	1.291	8.965	44497	0.005
2.9	0.822	1.211	9.065	33060	0.005
2.9	0.864	1.120	9.088	7681	0.011
2.9	0.935	0.937	8.977	1081	0.030
2.9	0.988	0.938	9.302	24411	0.006
3.4	0.187	3.939	1.737	220156	0.002
3.5	0.225	3.576	2.739	580748	0.001
3.5	0.274	3.164	4.159	496646	0.001
3.5	0.324	2.838	5.207	385231	0.002
3.5	0.373	2.575	5.946	300787	0.002
3.5	0.424	2.352	6.549	223570	0.002
3.5	0.474	2.161	7.042	169057	0.002
3.5	0.525	1.988	7.427	145158	0.003
3.5	0.574	1.843	7.726	115398	0.003
3.5	0.624	1.707	7.989	82281	0.003
3.5	0.674	1.583	8.179	61568	0.004

Table 2 (continued): Expected relative statistical error on each data point within the kinematic coverage with 11 GeV beam energy (continued on next page).

$Q^2/(\mathrm{GeV}^2/c^2)$	x	W/GeV	E'/GeV	No. of Events	Rel. Stat. Err.
3.5	0.724	1.467	8.415	42904	0.005
3.5	0.773	1.360	8.538	29873	0.006
3.4	0.823	1.254	8.700	23614	0.007
3.5	0.867	1.167	8.762	11039	0.010
3.5	0.932	0.950	8.444	853	0.034
3.4	0.989	0.938	8.963	13429	0.009
3.9	0.195	4.108	1.403	8478	0.011
4.1	0.231	3.789	1.862	270060	0.002
4.1	0.274	3.432	2.880	395359	0.002
4.1	0.323	3.078	4.086	308526	0.002
4.1	0.374	2.786	4.992	236942	0.002
4.1	0.424	2.538	5.718	183681	0.002
4.1	0.474	2.326	6.273	134859	0.003
4.1	0.524	2.139	6.700	101855	0.003
4.1	0.574	1.972	7.093	85695	0.003
4.1	0.624	1.821	7.404	66746	0.004
4.1	0.673	1.682	7.657	48139	0.005
4.1	0.724	1.551	7.916	32719	0.006
4.1	0.772	1.433	8.073	21736	0.007
4.1	0.825	1.308	8.276	15534	0.008
4.1	0.870	1.208	8.363	10299	0.010
4.2	0.915	1.088	8.194	1365	0.027
4.1	0.990	0.938	8.606	6486	0.012
4.7	0.241	3.938	1.459	21964	0.007
4.9	0.279	3.661	1.920	210824	0.002
4.9	0.324	3.340	2.785	251339	0.002
4.9	0.374	3.015	3.834	195517	0.002
4.9	0.424	2.745	4.682	150507	0.003
4.9	0.474	2.510	5.341	111187	0.003
4.9	0.524	2.303	5.893	82110	0.003
4.9	0.574	2.115	6.323	57244	0.004
4.9	0.624	1.946	6.701	51098	0.004
4.9	0.674	1.794	7.039	40400	0.005
4.9	0.723	1.652	7.288	29020	0.006
4.9	0.773	1.508	7.518	18720	0.007
4.9	0.824	1.372	7.724	10811	0.010

Table 2 (continued): Expected relative statistical error on each data point within the kinematic coverage with 11 GeV beam energy (continued on next page).

$Q^2/(\mathrm{GeV}^2/c^2)$	x	W/GeV	E'/GeV	No. of Events	Rel. Stat. Err.
4.9	0.874	1.243	7.885	9161	0.010
5.1	0.913	1.154	7.906	1422	0.027
4.9	0.992	0.937	8.137	3357	0.017
5.6	0.288	3.820	1.493	18834	0.007
5.8	0.328	3.554	1.885	127120	0.003
5.9	0.374	3.269	2.547	155458	0.003
5.9	0.424	2.974	3.466	116878	0.003
5.9	0.474	2.713	4.293	87857	0.003
5.9	0.524	2.482	4.924	61682	0.004
5.9	0.573	2.282	5.422	44953	0.005
5.9	0.624	2.085	5.896	29646	0.006
5.9	0.675	1.909	6.292	27370	0.006
5.9	0.723	1.753	6.580	20883	0.007
5.9	0.772	1.603	6.808	14851	0.008
5.9	0.822	1.452	7.034	7909	0.011
5.9	0.874	1.299	7.264	5291	0.014
5.8	0.916	1.171	7.481	1763	0.024
5.8	0.993	0.937	7.581	1820	0.023
6.6	0.339	3.701	1.605	4381	0.015
6.8	0.380	3.453	1.900	48310	0.005
6.9	0.425	3.200	2.365	80232	0.004
7.0	0.474	2.937	2.992	69592	0.004
7.0	0.524	2.681	3.731	50529	0.004
7.0	0.574	2.458	4.395	36702	0.005
7.0	0.623	2.251	4.841	23500	0.007
7.0	0.674	2.053	5.476	16558	0.008
7.0	0.726	1.865	5.791	14168	0.008
7.0	0.773	1.701	6.094	10128	0.010
7.1	0.827	1.521	6.326	6486	0.012
7.0	0.875	1.359	6.540	3926	0.016
7.0	0.918	1.209	6.703	1138	0.030
7.0	0.994	0.937	6.864	739	0.037
7.9	0.395	3.584	1.748	455	0.047
8.0	0.433	3.361	1.935	8535	0.011
8.2	0.477	3.126	2.195	27882	0.006
8.3	0.525	2.890	2.667	34483	0.005

Table 2 (continued): Expected relative statistical error on each data point within the kinematic coverage with 11 GeV beam energy (continued on next page).

$Q^2/(\mathrm{GeV}^2/c^2)$	x	W/GeV	E'/GeV	No. of Events	Rel. Stat. Err.
8.4	0.574	2.655	3.149	25264	0.006
8.4	0.624	2.426	3.744	17696	0.008
8.4	0.673	2.218	4.273	13258	0.009
8.3	0.727	1.984	4.908	8535	0.011
8.4	0.774	1.815	5.168	8250	0.011
8.3	0.825	1.608	5.328	4381	0.015
8.4	0.872	1.438	5.789	2902	0.019
8.3	0.925	1.209	5.806	1138	0.030
8.5	0.995	0.935	5.991	455	0.047
9.4	0.487	3.270	2.190	512	0.044
9.5	0.530	3.042	2.261	4324	0.015
9.7	0.577	2.812	2.444	9502	0.010
9.8	0.625	2.598	2.755	11380	0.009
10.0	0.672	2.386	3.173	8763	0.011
9.9	0.725	2.145	3.596	6031	0.013
10.0	0.773	1.940	3.878	5405	0.014
9.8	0.818	1.737	4.560	1934	0.023
9.9	0.872	1.514	4.764	1479	0.026
10.0	0.922	1.303	4.867	569	0.042
10.0	0.978	1.029	4.820	113	0.094
11.2	0.583	2.966	2.484	113	0.094
11.2	0.628	2.718	2.639	398	0.050
11.4	0.674	2.514	2.695	1479	0.026
11.6	0.725	2.291	2.903	2788	0.019
11.7	0.772	2.072	3.015	1593	0.025
11.8	0.827	1.816	3.445	1194	0.029
11.7	0.874	1.590	4.040	625	0.040
11.4	0.916	1.382	4.422	227	0.066
11.3	0.998	0.934	4.656	113	0.094
13.6	0.738	2.368	2.705	56	0.133
13.9	0.791	2.098	3.319	56	0.133
13.4	0.826	1.909	2.765	113	0.094
13.2	0.861	1.731	3.262	56	0.133

Table 2 (continued): Expected relative statistical error on each data point within the kinematic coverage with 11 GeV beam energy.